nature communications

Article

https://doi.org/10.1038/s41467-025-58447-5

Injectable ECM-mimetic dynamic hydrogels abolish ferroptosis-induced post-discectomy herniation through delivering nucleus pulposus progenitor cell-derived exosomes

Received: 4 September 2024

Accepted: 21 March 2025

Published online: 01 April 2025

Check for updates

Wenkai Wang[1,2,5], Zhuo Cheng[1,5], Miao Yu[1], Ke Liu[1], Hongli Duan[1], Yang Zhang[1], Xinle Huang[1], Menghuan Li[3], Changqing Li[1], Yan Hu[4,6] ✉, Zhong Luo[3,6] ✉ & Minghan Liu[1,6] ✉

Discectomy-induced ferroptosis of nucleus pulposus cells (NPCs) contributes to postoperative lumbar disc herniation (LDH) recurrence and intervertebral disc degeneration (IDD). We discover that nucleus pulposus progenitor cells (NPPCs) could imprint ferroptosis resistance into NPCs through exosome-dependent intercellular transmission of miR-221-3p. Based on these findings, we first develop synthetically-tailored NPPC-derived exosomes with enhanced miR-221-3p expression and NPC uptake capacity, which are integrated into an injectable hydrogel based on extracellular matrix (ECM) analogues. The ECM-mimetic hydrogel (HACS) serves as a biomimetic filler for the post-operative care of herniated discs, which could be facilely injected into the discectomy-established nucleus pulposus (NP) cavity for localized treatment. HACS-mediated in-situ exosome release in the NP cavity enables marked ferroptosis inhibition in NPCs that not only prevents LDH recurrence but also reverses the IDD symptoms, leading to robust restoration of NP structure and functions. In summary, this study offers a promising approach for treating disc herniation.

Intervertebral disc degeneration (IDD) is one of the most prevalent degenerative musculoskeletal diseases, affecting approximately 5-10% of the global population across a broad age spectrum[1]. The progression of IDD often leads to disc herniation, characterized by the rupture of annulus fibrosus and the protrusion of nucleus pulposus (NP), leading to significant disability. Discectomy is currently the mainstream modality for treating disc herniation, during which the herniated discs are partially or completely removed to relieve the pressure[2]. However, clinical data consistently demonstrate that discectomy is associated with a high risk of recurrent intervertebral disc herniation and accelerated IDD progression[3,4]. Recent insights increasingly reveal that ferroptosis is one of the major drivers of IDD pathology[1,5,6]. Notably, these findings collectively highlight that NPC ferroptosis is a confirmed promotor of IDD by impairing the viability of NP-residing cells as well as damaging the extracellular matrix (ECM)[7,8], while the operation-induced physical and biochemical insults could significantly promote the ferroptosis cascades in NPCs to enhance the degenerative phenotype as well as aggravate the IDD symptoms. Therefore, reversing the ferroptosis programs in degenerative NPCs has emerged as a promising strategy to enable robust intervertebral

[1]Department of Orthopedics, Xinqiao Hospital, Third Military Medical University (Army Medical University), Chongqing, China. [2]Department of Orthopedics, General Hospital of PLA Xizang Military Area Command, Lhasa, Xizang, China. [3]School of Life Science, Chongqing University, Chongqing, China. [4]Key Laboratory of Biorheological Science and Technology, Ministry of Education, College of Bioengineering, Chongqing University, Chongqing, China. [5]These authors contributed equally: Wenkai Wang, Zhuo Cheng. [6]These authors jointly supervised this work: Yan Hu, Zhong Luo, Minghan Liu. ✉e-mail: huyan303@cqu.edu.cn; luozhong918@cqu.edu.cn; liuminghan@tmmu.edu.cn

disc (IVD) restoration and prevent recurrent lumbar disc herniation (rLDH).

Nucleus pulposus progenitor cells (NPPCs) are a group of cells derived from embryonic notochord and capable of differentiating into other NP-like cell populations, which have crucial roles in maintaining the functional integrity of healthy NPs[9–13]. In addition to their intrinsic capabilities to refresh NP cellularity, NPPCs also induce significant phenotypical changes in surrounding NPCs through establishing an intricate cell-cell communication network, during which they could export some of their progenitor-like properties into differentiated NPCs for maintaining their cellular hemostasis in the NP microenvironment[12]. Due to the avascular nature of the NP, resident cells experience a harsh microenvironment marked by pronounced hypoxia and limited nutrient supply[14]. Interestingly, previous reports collectively confirm that NPPCs are highly resistant to various forms of programmed cell death to withstand the NP-associated survival stress[9,12,15]. Indeed, there is substantial evidence that loss or exhaustion of NPPCs is a major cause of NPC dysfunction, leading to the onset of IDD pathogenesis and enhancing the risk of disc herniation[9]. Collectively, it is of clinical interest to explore the intercellular communication capabilities of NPPCs to regulate the ferroptosis cascade in degenerative IVDs.

Here we discover that NPPCs could secrete exosomes as messengers to transmit their ferroptosis resistance to other NPCs, which are extracellular nanovesicles containing various cell-derived cargos including cytokines, proteins, RNA and DNA and capable of mediating intercellular communication via an endocrine-like manner. Sequencing analysis further reveals that the exosome-enabled imprint of ferroptosis resistance on differentiated NPCs is mediated by the enclosed miR-221-3p microRNA components, which could inhibit the pro-ferroptosis interferon-regulatory factor 8 (IRF8)- signal transducer and activator of transcription 1 (STAT1) axis to upregulate solute carrier family 7 member 11 (SLC7A11) expression, thus boosting the lipid peroxide-scavenging capacity of glutathione peroxidase 4 (GPX4)-glutathione (GSH) system to rescue ferroptotic NPCs. These findings provide the mechanistic foundation for utilizing NPPC-derived exosomes as a potential strategy to reverse ferroptosis in herniated IVDs. To enhance the clinical translational potential of NPPC-derived exosomes, we develop a multi-level exosome engineering strategy to amplify their anti-ferroptosis capacity. Specifically, NPPCs are first treated with miR-221-3p-expressing adenovirus vectors, and the harvested exosomes are then modified with a cell-penetrating peptide (CPP) ligand, leading to significant enhancement in the miR-221-3p loading as well as the NPC uptake efficacy. Extending from the physical and biochemical properties of the engineered NPPC-derived exosomes, we further develop an injectable hydrogel filler based on clinically-tested ECM analogs including hyaluronic acid (HA) and oxidized chondroitin sulfate (OCS) as the exosome delivery platform (HACS@CPP-miR-Exo) for post-discectomy management, which is not only well tolerated in the operation-induced NP cavity but also enables sustainable release of the engineered exosomes to mediate continuous ferroptosis reversal in NPCs (Fig. 1a). In vitro and in vivo analysis consistently support that the exosome-integrated hydrogel systems are well-tolerated in post-discectomy NPs and efficiently restore the redox homeostasis in ferroptotic NPCs through marked inhibition of the IRF8-STAT1 program (Fig. 1b), leading to robust regeneration of healthy NP without negligible risk of rLDH (Fig. 1c). Overall, our study provides a clinically translatable strategy to overcome the current challenges in the treatment of lumbar disc herniation.

Results

Ferroptosis of NPCs drives post-discectomy disc herniation and degeneration

To investigate the contributing factors of post-discectomy rLDH and IDD degeneration, we screened the gene expression omnibus (GEO) database of human IVD and selected GSE70362 dataset. This dataset was regrouped into the control (grade I and II) and IDD (grade IV and V) groups according to the Thompson grading system[16]. Principal-component analysis (PCA) indicated that biological replicates within the same group clustered together, confirming the validity of the sample rearrangement (Fig. 2a). Among 1777 differentially expressed genes (DEGs, $|\log_2 FC| > 2$, $P < 0.05$) of the NP tissues in IDD group, 651 genes (36.6%) were upregulated compared with healthy NPs, whereas 1126 genes (63.4%) were downregulated (Fig. 2b, c). Gene Ontology (GO) and Kyoto Encyclopedia of Genes and Genomes (KEGG) analyses were performed to functionally classify these DEGs (Fig. 2d, e). According to the GO analysis, the expression of genes associated with "phospholipid metabolic process", "oxidative stress", and "regulation of metal ion transport" were significantly elevated in the degenerated NP, indicating the activation of lipid peroxidation (Fig. 2d). It is universally acknowledged that lipid peroxidation and iron-dependent accumulation contributed to ferroptosis. Furthermore, KEGG analysis revealed that ferroptosis-associated metabolic and signaling pathways, including "Arachidonic acid metabolism", "Cholesterol metabolism", "Fatty acid degradation", "Lipid and atherosclerosis", and "p53 signaling" were significantly upregulated in degenerative NPs (Fig. 2e). Additionally, Gene Set Enrichment Analysis (GSEA) showed that pro-ferroptosis gene sets were upregulated in the degenerative NPs (Fig. 2f). These results demonstrated that the aberrant activation of ferroptosis program is a major contributing factor to NPC degeneration.

To study whether the NPC ferroptosis enhances the risk of post-discectomy rLDH and IDD, we performed discectomy on the caudal IVDs of rats and observed the biochemical alterations in the affected IVDs throughout an 8-week period. NP samples were extracted to examine the time-dependent changes in oxidative stress and lipid peroxidation levels following discectomy (Fig. 2g). Quantitative real-time polymerase chain reaction (qPCR) analysis indicated that the mRNA expression levels of ferroptosis promotors such as *Cybb*, *Nox4*, *Acsl4*, and *TP53* gradually increased in the NP tissue over time (Fig. 2h). In contrast, the mRNA expression of the anti-ferroptosis enzyme glutathione peroxidase 4 (GPX4) significantly decreased after discectomy. These trends were consistent with the protein expression levels of acyl-CoA synthetase long chain family member 4 (ACSL4) and GPX4 according to western blot and immunohistochemical staining (Fig. 2i, j; Supplementary Fig. 1a, b). Analysis on the ferrous ions (Fe^{2+}) and NP-intrinsic lipid peroxidation levels revealed a similar pattern, where the Fe^{2+} and malondialdehyde (MDA) abundance in the post-discectomy NP tissues steadily increased over time (Fig. 2k, l). These results demonstrate that discectomy-induced stress may exacerbate ferroptosis of the post-operative NP, thereby promoting degenerative phenotypes in NPCs and impairing the treatment efficacy against the herniated discs. To determine the relative contribution of ferroptosis to post-discectomy IDD pathophysiology, we tested the ameliorative effect of various cell death inhibitors on degenerative IVDs for comparative analysis including apoptosis inhibitor ZVAD-FMK, pyroptosis inhibitor Necrosulfonamide and ferroptosis inhibitor Ferrostatin-1. The results not only revealed the involvement of both apoptosis and pyroptosis programs for driving IVD degeneration but also confirmed that ferroptosis is the primary contributor to the post-discectomy degeneration of IVDs, evidenced by the much superior degeneration amelioration effect of Ferrostatin-1 than ZVAD-FMK and Necrosulfonamide thereof (Fig. 2m, n).

To further investigate the link between ferroptosis and IDD post-discectomy, we administered anti-ferroptosis treatments using Ferrostatin-1 and Deferoxamine. Two weeks post-discectomy, rats were treated with Ferrostatin-1 and Deferoxamine for an additional two weeks. Notably, anti-ferroptosis treatment led to a significant reduction in histological degeneration grades compared to the model group, suggesting effective reversal of IDD following

discectomy (Supplementary Fig. 1c, d). Furthermore, the immunohistochemical analysis demonstrated a marked increase in aggrecan and a decrease in matrix metallopeptidase 13 (MMP13) in the IVDs following Ferrostatin-1 and Deferoxamine treatment, both of which are typical markers of degenerative IVDs (Supplementary Fig. 1c, e). These findings collectively suggest that ferroptosis contributes to post-discectomy IDD and that alleviating ferroptosis in degenerative NPCs may represent a promising therapeutic strategy for IDD treatment.

NPPC-derived exosomes imprint ferroptosis resistance in NPCs

Extending from the intrinsic ferroptosis resistance of NPPCs and their regulatory capacities for maintaining redox homeostasis in NP, we investigated the phenotypical signatures and intercell communication

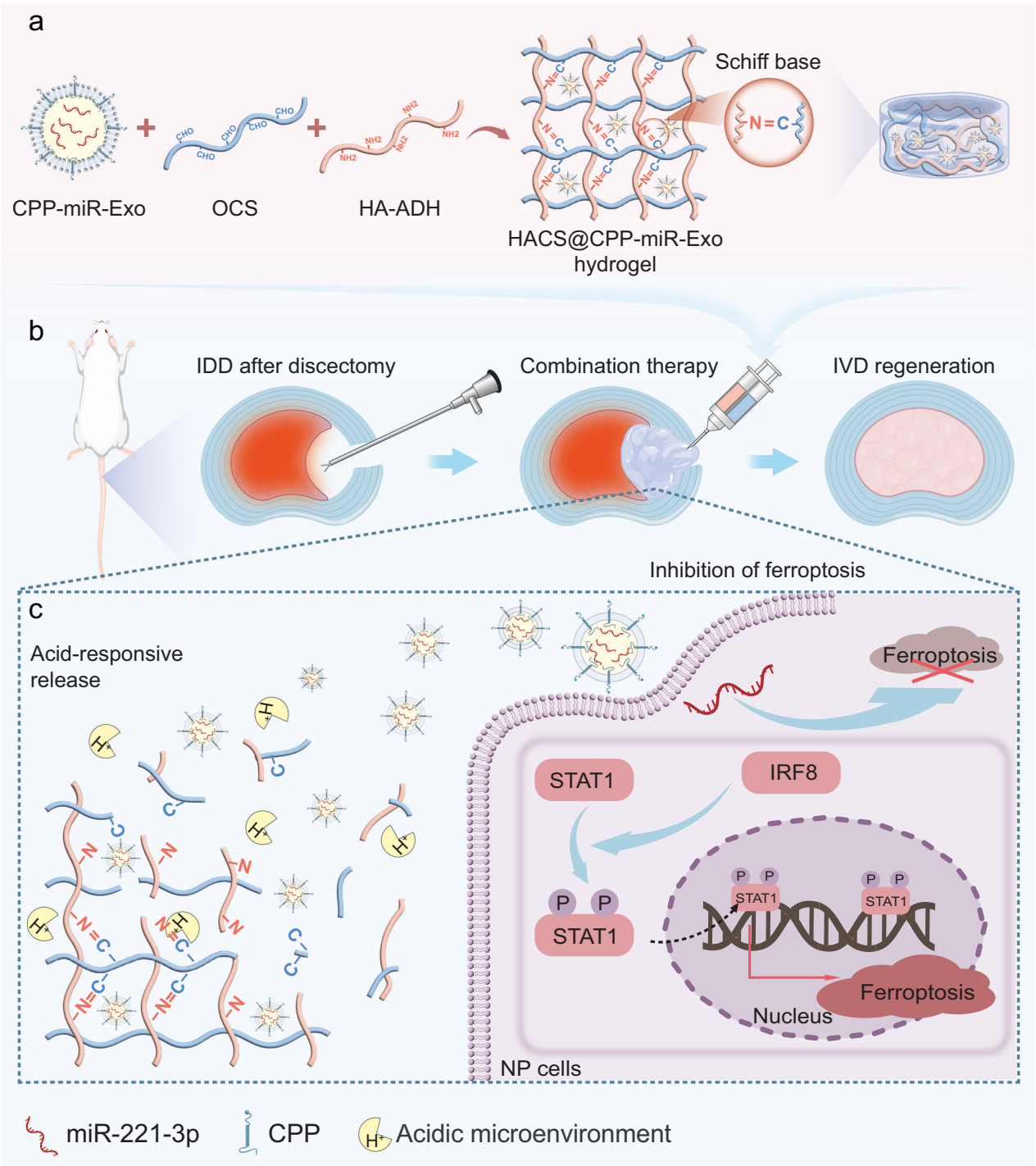

Fig. 1 | Schematic illustration of the development of the hydrogel components for post-discectomy care of IVDs. a Engineering process of NPPC-derived exosomes and their incorporation into the injectable hydrogel based on ECM analogs. **b** A sketch showing treatment of IDD rats by HACS@CPP-miR-Exo. **c** The HACS@CPP-miR-Exo therapy potently inhibits the ferroptosis programs in NPCs through leveraging IRF8-STAT1 pathway, leading to enhanced post-discectomy IVD recovery. OCS oxidized chondroitin sulfate, HA-ADH adipic acid dihydrazide-modified hyaluronic acid, CPP cell-penetrating peptide, CPP-miR-Exo miR-221-3p overexpressed NPPC-derived exosomes with CPP modification, IRF8 interferon-regulatory factor 8, STAT1 signal transducer and activator of transcription 1. Schematic illustrations were generated using BioRender (Wang, V., 2025; accessible at: https://BioRender.com/i62o243). Source data are provided as a Source Data file.

https://doi.org/10.1038/s41467-025-58447-5

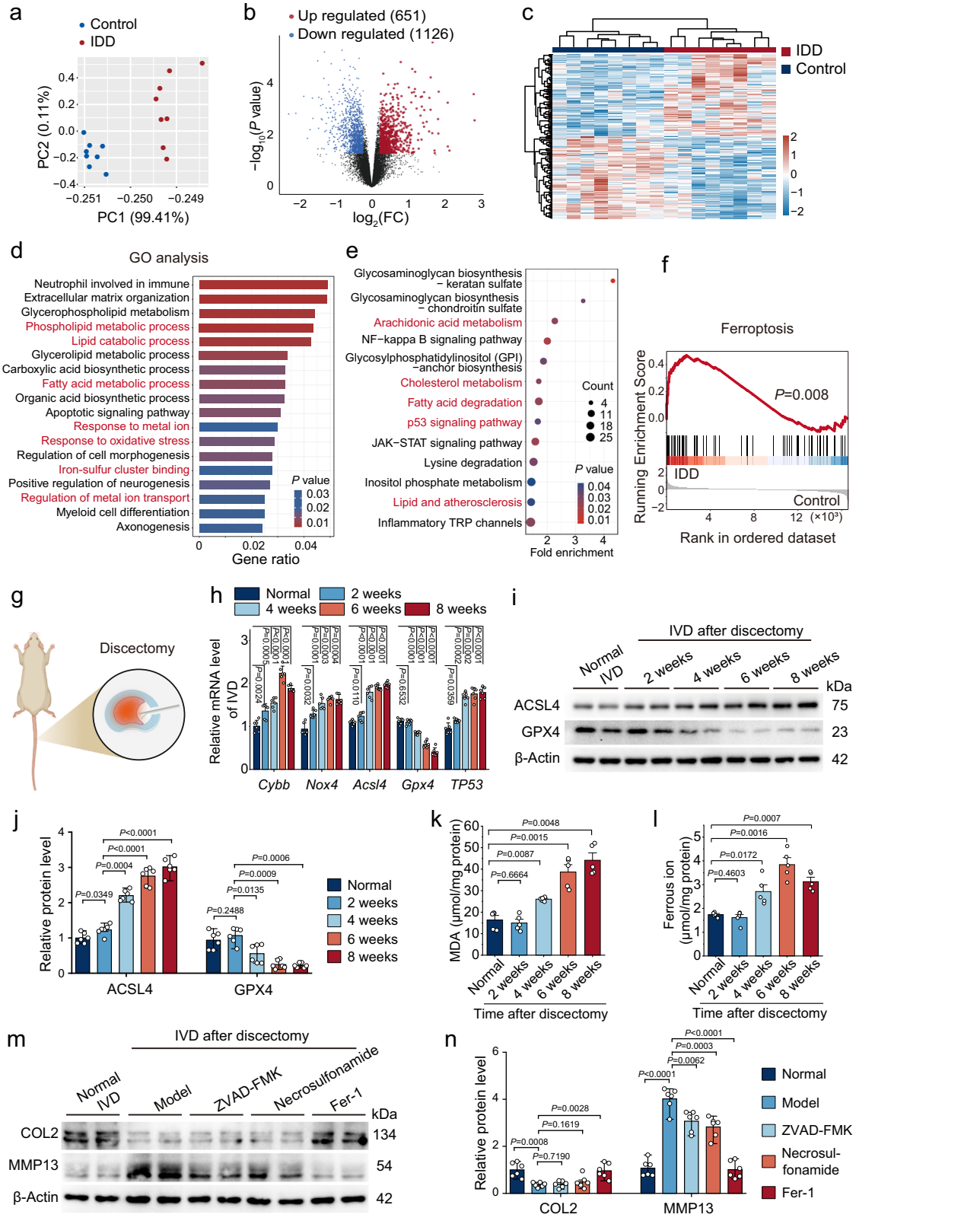

pathways of NPPCs for studying their potential impact on NPC ferroptosis through intercellular communication. For this purpose, we first isolated NPPCs from newborn rats and profiled their progenitor-associated characteristics via immunofluorescence staining and flow cytometry (Fig. 3a–c). Typically, the extracted healthy NPPCs showed positive expression status of mesenchymal stem cell-related markers like CD44, CD29, CD90, CD73, and CD105, while the expression of CD45, CD11b, and CD34 were at low levels, which confirmed the progenitor properties of NPPCs under normal conditions and were in line with their ferroptosis resistance[17,18].

Exosomes serve as crucial intercellular messengers and have been implicated in the regulation of ferroptosis across a myriad of biological systems[19,20]. Accordingly, we subsequently extracted NPPC-derived exosomes to study their impact on the ferroptosis programs in NPCs.

Fig. 2 | Post-discectomy ferroptosis of NPCs promotes IDD. a–f Analysis of RNA sequencing data from human intervertebral discs (GSE70362) obtained from the Gene Expression Omnibus (GEO) database. **a** Principal Component Analysis (PCA) of the reorganized samples from GSE70362. **b** Volcano plot illustrating the DEGs between the two groups. The significant DEGs were filtered with thresholds of a | log_2(fold change, FC)| > 2 and *P* value < 0.05 using the R package DESeq2. **c** Heatmap showing significant DEGs between the control and degenerative NPs. **d** Gene Ontology (GO) analysis of the RNA-seq results. **e** Kyoto Encyclopedia of Genes and Genomes (KEGG) analysis of the RNA-seq results. **f** Gene Set Enrichment Analysis (GSEA) of gene sets related to ferroptosis for the control and degenerative NPs. **g–j** Evaluation of ferroptosis-related markers in IVDs of rats at various time points post-discectomy. **g** Diagram depicting the discectomy procedure in rats. **h** qRT-PCR analysis of typical ferroptosis-related markers in the IVDs post-discectomy ($n = 6$ independent rats). The expression of ACSL4 and GPX4 (**i**) and associated quantitative analysis (**j**) in IVD after discectomy ($n = 6$ independent rats). **k–l** Malondialdehyde (MDA) and ferrous ion levels in the IVD at different time points post-discectomy ($n = 5$ independent rats). The expression of COL2 and MMP13 (**m**) and associated quantitative analysis (**n**) in IVD after discectomy ($n = 6$ independent rats). In panels (**d–f**) the gene enrichment analysis was performed using the hypergeometric test with multiple testing correction. Comparisons were performed by two-tailed Student's t test in panels (**h**, **j**, **k**, **l** and **n**). Data are presented as means ± SD. DEGs Differentially Expressed Genes, IVD intervertebral disc, IDD intervertebral disc degeneration, ACSL4 acyl-CoA synthetase long chain family member 4, GPX4 glutathione peroxidase 4, COL2 Collagen II, MMP13 matrix metallopeptidase 13, ZVAD-FMK a pan caspase inhibitor, Fer-1 ferrostatin-1. Schematic illustrations were generated using BioRender (Wang, V., 2025; accessible at: https://BioRender.com/i62o243). Source data are provided as a Source Data file.

After culturing and proliferating NPPCs, NPPC-secreted exosomes (NPPC-Exo) were isolated from the supernatant for further analysis (Supplementary Fig. 2). Transmission electron microscopy (TEM) revealed that NPPC-Exo exhibited the characteristic spherical morphology (Fig. 3d). Dynamic light scattering measurements showed that NPPC-Exo had an average diameter of 118.2 ± 16.2 nm (Fig. 3e). Western blot analysis confirmed the presence of typical exosomal markers including TSG101, ALIX, CD63, and CD9 in NPPC-Exo (Fig. 3f; Supplementary Fig. 3), These data collectively supported the successful extraction of NPPC-Exo.

Furthermore, by labeling the NPPC-Exo with PKH26 probes, we observed that NPPC-Exos were rapidly internalized by NPCs, further substantiating their functions as a communication messenger between NPPCs and NPCs (Fig. 3g). To investigate the potential regulatory effects of NPPC-Exos on ferroptotic NPCs ferroptosis, we first induced ferroptosis in NPCs using Erastin, which is a broadly used ferroptosis inducer with good biostability and biological representativeness[21]. Notably, 1 μM of Erastin was sufficient to induce significant ferroptosis in NPCs after 24 h of incubation (Supplementary Fig. 4). Subsequently, we analyzed the impact of NPPC-Exos and NPC-derived exosomes (NPC-Exos) on Erastin-induced ferroptotic NPCs. NPPC-Exo treatment effectively reduced intracellular reactive oxygen species (ROS) and lipid peroxide (LPO) generation in ferroptotic NPCs (Supplementary Fig. 5a, b; Fig. 3h, i), along with a marked reduction in intracellular iron concentration based on FerroOrange assays (Fig. 3j, Supplementary Fig. 5c). Consistent with the biochemical alterations above, NPPC-Exo-treated NPCs exhibited an obvious decrease in the total amount of ferroptosis-associated condensed mitochondria (Supplementary Fig. 5d, e). In contrast, NPCs in the Erastin+NPC-Exo group maintained the typical ferroptotic features including high levels of ROS and lipid peroxidation, abundant cellular iron deposition and obvious mitochondrial alterations, all of which were at a similar level to the Erastin only group. Collectively, these results demonstrate that NPPC-Exo, rather than NPC-Exo, can rescue ferroptotic NPCs through reversing the ferroptosis programs. Moreover, to identify whether there were other intercellular communication modalities involved in NPPC-dependent anti-ferroptosis activities, we established transwell co-incubation system of NPPCs (upper chamber) and degenerative NPCs (bottom chamber). Treating NPPCs with exosome secretion inhibitor GW4869 almost abolished the NPPC-mediated anti-ferroptosis effects on NPCs. Similarly, removing exosomal contents in NPPC-conditioned culture media via ultra-speed centrifugation also abrogated their ferroptosis inhibition capability on NPCs. These observations validated our hypothesis that the NPPC-secreted exosomes are the primary intercellular communication modality for imprinting their ferroptosis resistance into degenerative NPCs (Fig. 3k, Supplementary Fig. 5f, g).

miR-221-3p is the anti-ferroptosis effector molecule in NPPC-Exo

Exosomes are extracellular vesicles enclosing various types of proteins, lipids, and nucleic acids. Recent studies increasingly revealed microRNAs (miRNAs) as crucial mediators of exosome-dependent intercellular communication[22]. Indeed, several exosome-associated miRNAs are implicated in ferroptosis regulation with significant promotional or inhibitory roles, of which the notable examples include miR-3173-5p, miR-144-3p, miR-125b-5p, and miR-129-5p[23–26]. To investigate the key effectors in NPPC-Exo-mediated anti-ferroptosis effects, we compared miRNA expression profiles in NPPC-Exos and NPC-Exos using miRNA sequencing (Fig. 3l–n). A total of 46 miRNAs were upregulated, while 24 miRNAs were downregulated in NPPC-Exos compared to NPC-Exos (Fig. 3m). Among the differentially up-regulated miRNAs, we selected miR-16-5p, miR-146a-5p, miR-221-3p, and miR-181d-5p for further investigation based on their expression levels and early studies (Fig. 3n)[27–31] and synthesized corresponding anti-miRNA oligonucleotides (AMOs) for investigating their ROS-regulatory effects. Surprisingly, only anti-miR-221-3p treatment induced significant attenuation of NPPC-Exo-mediated ROS elimination (Fig. 3o, Supplementary Fig. 6a), suggesting that miR-221-3p is the major contributor to the anti-ferroptosis effects of NPPC-Exo. Indeed, qPCR analysis indicated that the miR-221-3p level in Erastin-induced degenerative NPCs was 50% lower than the Erastin-free healthy NPCs (Supplementary Fig. 7), further validating the correlation between intracellular miR-221-3p levels and ferroptosis-associated degenerative NPC phenotype.

After confirming the anti-ferroptosis contribution of miR-221-3p, we further developed miR-221-3p overexpressed NPPC-Exos (miR-Exo) through genetic engineering to enhance their efficacy in rescuing NPCs. For this purpose, we constructed a miR-221-3p adenovirus (AdV) vector for NPPC transfection (Supplementary Fig. 6b) to enhance miR-221-3p loading in NPPC-Exos (Fig. 3p). Here the ferrous ion contents, lipid peroxidation, and MDA levels in degenerative NPCs after miR-Exo treatment was comprehensively investigated via FerroOrange fluorescent probes, C11 BODIPY fluorescent probes, and MDA Assay Kit, respectively, both of which are widely employed for detecting lipid peroxidation in cells and tissues. The results demonstrated that miR-221-3p treatment substantially ameliorated the ferrous ion accumulation and lipid peroxidation in degenerative NPCs while reducing MDA expression, of which the relative reduction was 30%, 50%, and 40% according to quantitative analysis of the flow cytometry and confocal microscopy, affirming the anti-ferroptosis efficacy of NPPC-Exo on NPCs (Supplementary Fig. 6c–g). The miR-Exo treatment in ferroptotic NPCs also induced significant reductions in the number of damaged mitochondria (Supplementary Fig. 6i. j). Consistently, western blot analysis revealed that miR-Exo treatment more effectively upregulated the expression of Collagen II (COL2) and GPX4 while inhibiting ACSL4 in Erastin-conditioned NPCs than NPPC-Exo (Fig. 3q, Supplementary Fig. 6h). Moreover, TEM examination demonstrated that miR-Exo significantly ameliorated mitochondrial damage induced by ferroptosis, in contrast to both the model and NPPC-Exo groups (Supplementary Fig. 6i, j). These results collectively substantiate the superior ferroptosis rescue effect of miR-Exo on ferroptotic NPCs than pristine

https://doi.org/10.1038/s41467-025-58447-5

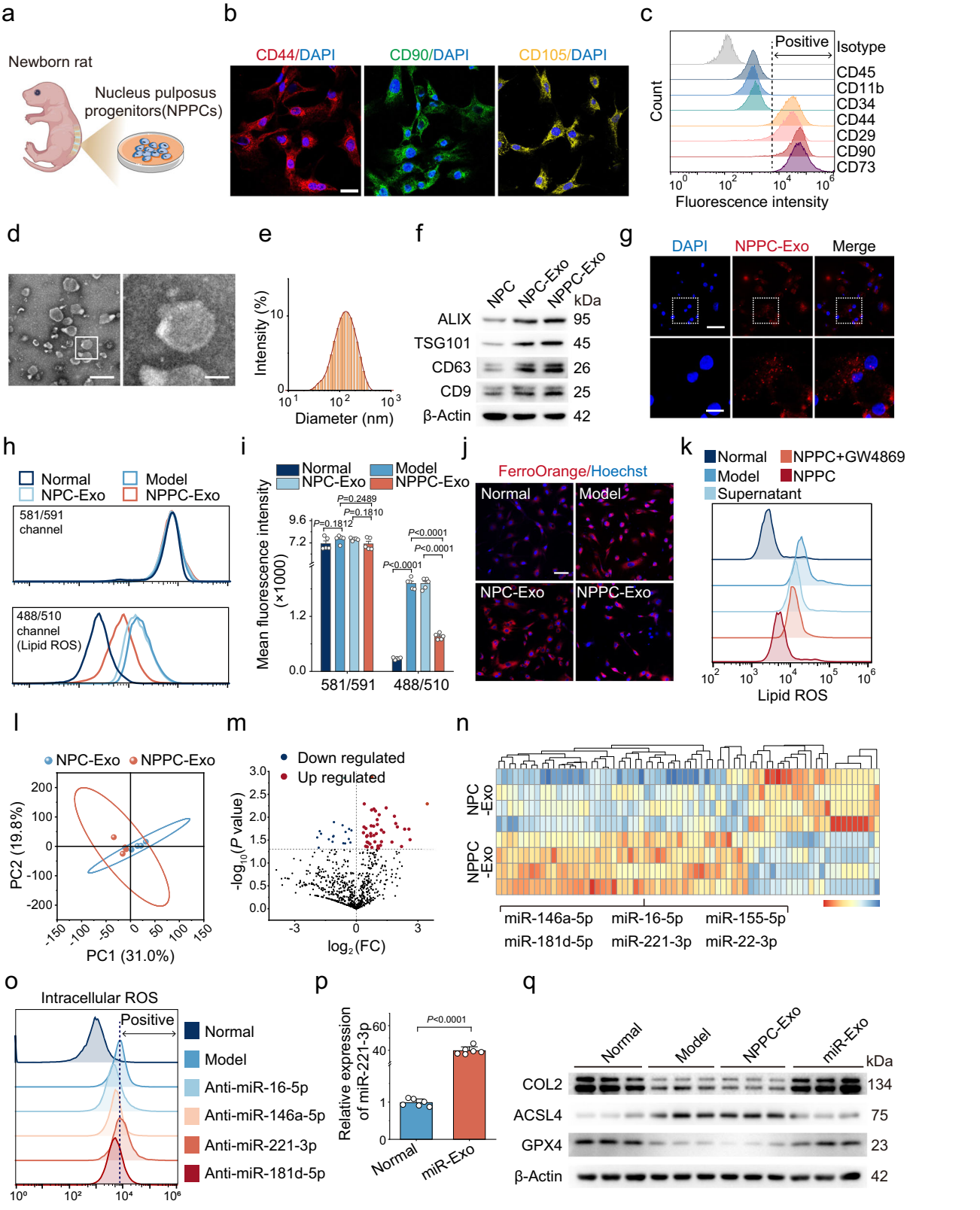

NPPC-Exo through enhancing the exosomal loading of anti-ferroptosis miR-221-3p.

Previous studies collectively demonstrate that miR-221-3p could not only inhibit the degeneration-associated ferroptosis signaling but also have potent anti-inflammatory capabilities[31–33]. Considering that postoperative IDD is frequently accompanied with chronic inflammation responses, we examined the biochemical alterations in NPPC-Exo-treated degenerative NPCs to comprehensively explore its IDD treatment mechanisms. NPPC-Exo treatment induced significant reduction in IL-1β secretion by degenerative NPCs that was almost comparable to clinically prescribed celecoxib-dependent IDD therapy, immediately suggesting the treatment-induced amelioration of IVD inflammation and may contribute to the IDD reversal efficacy. However, NPPC-Exo showed much superior degeneration reversal efficacy

Fig. 3 | NPPC-derived exosomes inhibited NPC ferroptosis through miR-221-3p delivery. a Schematic representation of NPPC isolation. **b** Immunofluorescence images on MSC marker expression including CD44, CD90, and CD105 in isolated NPPCs. Scale bar, 50 μm. **c** Flow cytometric analysis on CD45, CD11b, CD34, CD44, CD29, CD90, and CD73 expression in isolated NPPCs. **d** TEM images of NPPC-Exos. Scale bars, 200 nm (left) and 40 nm (right). **e** DLS analysis on NPPC-Exo size distribution. **f** WB analysis on exosomal marker expression in NPC-Exo and NPPC-Exo. **g** Fluorescence images showing the PKH26-labeled NPPC-Exo internalization by NPCs after 4 h of incubation. White square regions are magnified and shown in the lower panels. Scale bars, 200 μm (upper) and 50 μm (lower). Flow cytometric analysis (**h**) and quantification (**i**) of BODIPY™ 581/591 C11-stained NPCs from different groups. **j** FerroOrange fluorescence assay on ferrous ion abundance in NPCs from different groups. Scale bar, 200 μm. **k** Flow cytometric profiles of lipid ROS in NPCs after different treatment. miRNA sequencing analysis of NPPC-Exo and NPC-Exo. PCA plot (**l**) volcano plot (**m**) and heatmap (**n**) show the differentially expressed miRNAs in between. **o** Flow cytometric profiles of intracellular ROS in NPCs after treatment with different anti-miRNA oligonucleotides. **p** qRT-PCR analysis on miR-221-3p abundance in NPPC-Exo isolated from miR-221-3p-expressing adenovirus-transfected NPPCs. **q** Western blot bands of ferroptosis-associated proteins in rat NPs. In (**h**–**j**) and (**q**) NPCs were treated with 50 μg/mL exosomes. $n = 3$ independent experiments for panels (**b**, **c**, **d**, **e** and **g**). $n = 6$ independent experiments for panels (**f**, **p**) and (**q**). $n = 5$ independent experiments for panels (**i**, **j**). Comparisons were performed by two-tailed Student's t test in panels (**i**, **m** and **p**). Data are presented as means ± SD. NPC-Exo NPC-derived exosomes, NPPC-Exo NPPC-derived exosomes, ALIX ALG-2-interacting protein 1, TSG101 tumor susceptibility gene 101 protein, GW4869 exosome secretion inhibitor, miR-Exo miR-221-3p overexpressed NPPC-Exo, COL2 Collagen II, ACSL4 acyl-coenzyme A synthetase long-chain family member 4, GPX4 Glutathione Peroxidase 4. Schematic illustrations were generated using BioRender (Wang, V., 2025; accessible at: https://BioRender.com/i62o243). Source data are provided as a Source Data file.

than celecoxib treatment, evidenced by the augmented restoration of collagen II (*Col2*) and Aggrecan (*Acan*) expression in NPCs by 50 and 30%. Contrastingly, while showing significant anti-inflammation effect on degenerative NPCs, celecoxib failed to alleviate Erastin-induced degeneration of NPCs due to the lack of anti-ferroptosis capability (Supplementary Fig. 6k, l). These findings not only confirmed the anti-inflammation effect of miR-221-3p and its contribution to the NPPC-Exo-mediated IDD reversal, but also validated our hypothesis that NPPC-Exo abolished post-discectomy IDD predominantly through miR-221-3p-mediated inhibition of the ferroptosis program in degenerative NPCs.

Anti-ferroptosis mechanism of NPPC-Exo

To elucidate the ferroptosis rescue mechanism of miR-221-3p, we performed RNA sequencing on NPCs treated with NPPC-Exo or miR-Exo (Fig. 4a–d), which revealed that NPPC-Exo treatment could markedly downregulate IRF family genes in NPCs, suggesting the potential contribution of IRF signaling to the exosome-mediated ferroptosis inhibitory effects thereof. Meanwhile, we screened the potential downstream gene targets of miR-221-3p in miRWalk and TargetScan databases, which revealed that the miR-221-3p treatment induced obvious alterations in the expression levels of typical ferroptosis regulatory genes including *Atf3*, *Foxo1*, and *Foxo4* as well as the IRF family genes. Notably, the IRF family genes are found at the intersection of key DEGs from the transcriptome sequencing and integrated bioinformatic analysis, immediately suggesting their relevance to the ferroptosis-induced degeneration of NPCs than other miR-221-3p-regulated ferroptosis mediatory genes. Interestingly, luciferase reporter assay showed that the binding between miR-221-3p and 3' untranslated region (UTR) region of *Irf8* mRNA sequence was the strongest among all IRF family members, revealing the potential regulatory relationship between miR-221-3p and *Irf8* thereof (Fig. 4e). Specifically, co-transfection of miR-221-3p mimics with the wild-type reporter plasmids in HEK293T cells significantly decreased the luciferase activity, which was reversed when co-transfected with two mutant reporter plasmids (Fig. 4f). These results indicate that miR-221-3p from NPPC-Exo binds with high affinity to the 3'UTR region of *Irf8* mRNA, leading to post-transcriptional inhibition of its expression. Notably, administration of anti-miR-221-3p restored IRF8 expression in NPCs treated with miR-Exo according to western blot analysis (Fig. 4g, h), further confirming that IRF8 is a critical downstream target of miR-221-3p for ferroptosis amelioration. On the other hand, RNA sequencing data of degenerative NPCs treated with miR-Exo showed significant enrichment of the PI3K-AKT and JAK-STAT pathways among the DEGs (Supplementary Fig. 8a), corroborating the role of the STAT-dependent ferroptosis cascade as the primary driver of NPC degeneration in the context of post-discectomy IDD while also implying its regulatory linkage to miR-221-3p[34–37]. Therefore, we carried out integrative bioinformatic analysis to further elucidate the molecular mechanism underlying miR-221-3p-mediated IRF8 inhibition and STAT deactivation in ferroptotic NPCs. According to STRING database[38], the interaction between IRF8 and STAT1 was the greatest among all key members of the PI3K-AKT and JAK-STAT pathways (Supplementary Fig. 8b). STAT1 is a pivotal signaling molecule in the JAK-STAT pathway implicated in ferroptosis regulatory network[39], as phosphorylated STAT1 enhances the expression of ACSL4 and inhibits the expression of SLC7A11, thus facilitating ferroptosis-associated lipid peroxidation[35]. Meanwhile, recent reports also indicate that IRF8 can stimulate STAT1 phosphorylation[40–42]. The results identified that IRF8 was the major driver of STAT1 activation in ferroptotic NPCs, supporting the potential utility of miR-221-3p for alleviating NPC ferroptosis through inhibiting IRF8-STAT1 axis.

To test this hypothesis, we detected the expression of COL2, GPX4, STAT1, and phosphorylated STAT1 via western blot assays. The results showed that miR-Exo treatment reversed the Erastin-induced increases in NPC-intrinsic STAT1 phosphorylation (Fig. 4i, j). To elucidate the exact mechanism of the exosome treatment-induced inhibition on STAT1 phosphorylation, we conducted rescue experiments using anti-miR-221-3p. miR-Exo showed similar effect to STAT1 inhibitor Fludarabine, a STAT1 inhibitor to block the phosphorylation of STAT1and promote the expression of COL2, GPX4, and SLC7A11, eventually leading to pronounced anti-ferroptosis effects (Fig. 4k, l). Contrastingly, treatment ferroptotic NPCs with anti-miR-221-3p exacerbated ferroptosis. These observations immediately confirmed the critical role of miR-221-3p in inhibiting STAT1 phosphorylation associated ferroptosis.

In view of the intrinsic complexity in the composition and biological functions of stem cell-derived exosomes, we further carried out comprehensive analysis to delineate their ferroptosis regulatory mechanisms in addition to their modulatory effect on IRF8-STAT1 signaling pathway. KEGG enrichment analysis on the transcriptomic data of miR-Exo-treated NPCs showed marked alterations in multiple ferroptosis regulatory pathways including PI3K-Akt, MAPK, and IL17 in addition to the JAK-STAT axis, suggesting the capacity of NPPC-Exo treatment to affect multiple ferroptosis-associated signaling pathways in NPCs (Supplementary Fig. 9). Indeed, the miR-Exo-treated NPCs showed significantly lower expression of typical pro-ferroptosis genes including *TP53, Alox12, Atg5, Atg7, Tfr1, Sat1, Gls2*, and *Vdac2* than those counterparts of degenerated NPCs, accompanied with marked upregulation in ferroptosis suppressor genes including *Gpx4* and *Slc7a11* (Supplementary Fig. 10a). These trends were further validated by qPCR analysis on the mRNA levels of key ferroptosis mediators after different treatment (Supplementary Fig. 10b). Of note, the miR-Exo treatment induced substantial inhibition of p53 signaling activity in NPCs while promoting SLC7A11 expression (Supplementary Fig. 10c, d). In summary, these data collectively supported that the NPPC-Exo could not only stimulate the IRF8-STAT1 signaling but also simultaneously regulate multiple other ferroptosis pathways, thus cooperatively

https://doi.org/10.1038/s41467-025-58447-5

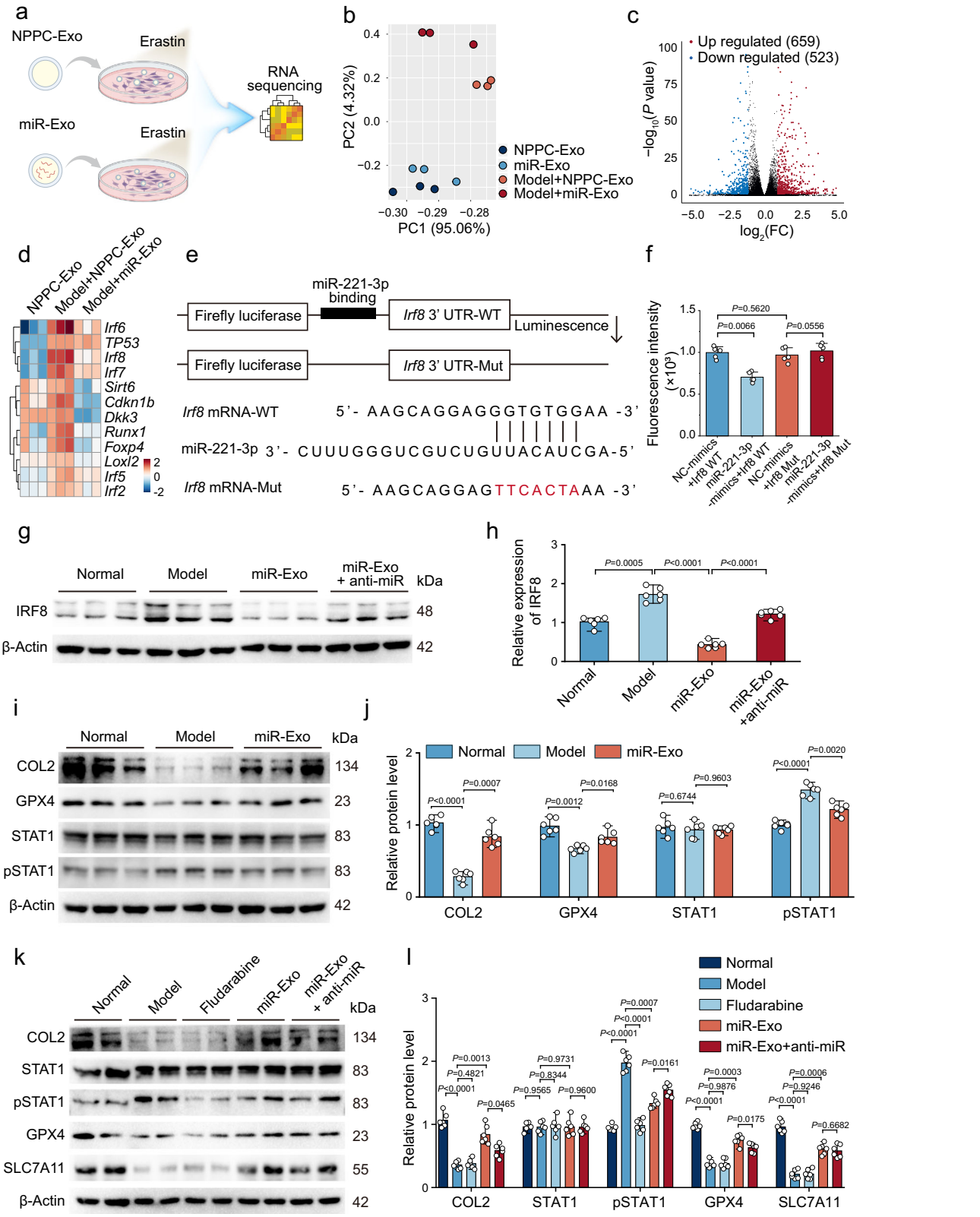

boosting the ferroptosis resistance of NPCs and further adding to the post-discectomy IDD treatment efficacy. On the other hand, Gene Set Enrichment Analysis (GSEA) based on the RNA sequencing data of miR-Exo-treated degenerative NPCs showed that NPPC-derived exosomes also potently inhibited the apoptotic and pyroptotic pathways (Supplementary Fig. 11) in addition to their ferroptosis inhibition effect, which was in line with the comparative analysis results on cell death inhibitor-mediated IDD rescue effect.

Engineering of the NPPC-derived exosomes

Cell-targeted delivery of bioactive nucleic acid therapeutics remains a major challenge in clinical practice due to their inherently low

Fig. 4 | miR-221-3p alleviates ferroptosis in NPCs by inhibiting IRF8-STAT1 axis. **a** RNA sequencing of NPCs following treatment with NPPC-Exo or miR-221-3p overexpressed NPPC-Exo (miR-Exo, 50 μg/mL). PCA analysis (**b**) volcano plot (**c**) and heatmap (**d**) demonstrate significant DEGs among different groups ($n = 3$ biologically independent samples). The significant DEGs in panel (**b**–**d**) were filtered with thresholds of a $|\log_2(\text{fold change, FC})| > 2$ and P value < 0.05 using the R package DESeq2. **e** Sequence alignments of miR-221-3p and its target site in the 3′UTR of *Irf8*. **f** Luciferase reporter assay conducted on HEK293T cells treated with miR-221-3p mimic, overexpressing either *Irf8*-wildtype 3′UTR (*Irf8*-WT) or *Irf8*-mutant 3′UTR (*Irf8*-Mut), $n = 5$ biologically independent samples. Western blot bands (**g**) and quantitative analysis (**h**) of IRF8 protein levels in NPCs treated with miR-Exo with or without anti-miR-221-3p ($n = 6$ biologically independent samples). Normal: NPCs with no treatment; Model: NPCs treated with Erastin; miR-Exo: NPCs treated with Erastin and miR-221-3p overexpressed NPPC-Exo (50 μg/mL); miR-Exo + anti-miR: NPCs treated with Erastin, miR-221-3p overexpressed NPPC-Exo (50 μg/mL), and anti-miR-221-3p. Western blot bands (**i**) and quantitative analysis (**j**) of COL2, GPX4, STAT1, and STAT1 phosphorylation protein levels in NPCs treated with miR-221-3p overexpressed NPPC-Exo at 50 μg/mL ($n = 6$ biologically independent samples). Western blot bands (**k**) and quantitative analysis (**l**) of COL2, STAT1, STAT1 phosphorylation, GPX4, and SLC7A11 protein levels in NPCs treated with miR-Exo with or without anti-miR-221-3p ($n = 6$ biologically independent samples). Comparisons were performed by two-tailed Student's t test in panels (**f**, **h**, **j**, **l**). Data are presented as means ± SD. NPPC nucleus pulposus progenitor cell, NPPC-Exo NPPC-derived exosomes, miR-Exo miR-221-3p overexpressed NPPC-Exo, IRF8 interferon regulatory factor 8, COL2 Collagen II, ACSL4 acyl-coenzyme A synthetase long-chain family member 4, GPX4 Glutathione Peroxidase 4, STAT1 signal transducer and activator of transcription 1, SLC7A11 solute carrier family 7 member 11. Schematic illustrations were generated using BioRender (Wang, V., 2025; accessible at: https://BioRender.com/i62o243). Source data are provided as a Source Data file.

biostability and rapid clearance[43]. To address these challenges, We further engineered miR-Exos with transactivator of transcription (TAT) peptidic ligands on their surface via non-invasive approaches[44,45], which have clinically-tested cytoplasmic membrane-crossing capability and biocompatibility, making them ideal for improving exosome uptake by ferroptotic NPCs in clinical context. Specifically, TAT peptides were first modified with cholesterol- polyethylene glycol (PEG)-Maleimide through Michael addition reaction (Supplementary Fig. 12) and then fused onto exosomal membrane by exploiting the lipophilic properties of the cholesterol moiety, resulting in the efficient generation of CPP-miR-Exo (Fig. 5a-d). Confocal microscopy observations revealed marked co-localization of CPP ligands with the membrane compartments of miR-Exo (Fig. 5c, d). Transmission Electron Microscopy (TEM) (Fig. 5b) and dynamic light scattering analysis revealed that TAT modification induced a slight increase in exosomal diameter while reducing the total negative charge of the exosomes. These data immediately confirmed the successful incorporation of the TAT ligands onto the exosomal surface (Fig. 5e, f). Western blot analysis revealed that both miR-Exo and CPP-miR-Exo displayed high expression levels of exosomal markers including ALIX, TSG101, CD63, and CD9, suggesting that the TAT ligand incorporation did not affect the exosomal integrity (Fig. 5g, h). The therapeutic benefit of TAT modification was further tested in vitro using fluorescently labeled samples (Fig. 5i). Notably, the uptake efficiency of CPP-miR-Exo by NPCs was much higher than that of miR-Exo, evidenced by the stronger cellular red fluorescence at all time points (Fig. 5j). This trend was further confirmed by flow cytometric analysis of cellular fluorescence retention after different treatments (Fig. 5k-m). Overall, the observations above confirmed that engineered CPP-miR-Exos could be a robust miR-221-3p delivery platform for NPC treatment.

Preparation and characterization of exosome-loaded HACS hydrogel

Despite the significant potential of miR-221-3p-overexpressing CPP-miR-Exos for anti-ferroptosis therapy, their clinical translation is still impeded by the intrinsically low stability of exosomes and miRNAs in the biological environment[46–48]. For this purpose, here we prepared an injectable hydrogel based on ECM analogs including hyaluronic acid (HA) and chondroitin sulfate (CS) for CPP-miR-Exo delivery to post-discectomy IVDs. Specifically, we first oxidized CS using sodium periodate to obtain oxidized chondroitin sulfate (OCS) with abundant aldehyde groups (Supplementary Fig. 13a), while adipic acid dihydrazide-modified HA (HA-ADH) was synthesized via EDC/NHS coupling (Supplementary Fig. 13b). The as-synthesized OCS and HA-ADH were characterized by Fourier transform infrared (FTIR) and ^{1}H NMR spectroscopy (Supplementary Fig. 14). ^{1}H NM analysis of the hydrogel precursors revealed that the degree of oxidation of OCS was 76%, and the substitution rate of ADH on the HA was approximately 23%. Notably, the aldehyde groups in OCS could rapidly react with amino groups in HA-ADH through Schiff base ligation, leading to the immediate hydrogel formation under clinically relevant mild conditions (Fig. 6a–c), which was denoted as HACS hydrogel.

To determine the optimal parameters for HACS hydrogel formation in a biological environment, we systematically evaluated the gelling behavior of the precursors under different volume ratios, including their gelation speed, rheological properties, SEM morphology, and compression characteristics. The storage modulus (G′) of the hydrogels remained higher than the loss modulus (G″), indicating that the samples were in a gel state. Interestingly, we detected that the obtained hydrogels showed the greatest gelling speed (< 10 s) and the highest storage modulus when the HA-ADH/OCS ratio was 4:1 (Fig. 6 d, e). Meanwhile, SEM imaging of the hydrogels showed well-dispersed porous structures at this ratio (Fig. 6f, g), which could provide ample space for in-situ exosome delivery. Furthermore, the tightly cross-linked porous structure enabled robust mechanical properties to the hydrogels under clinically relevant conditions with 0.7 MPa (Fig. 6h). Considering that the IVD is in a constant compression-decompression cycle, it is also important to test anti-fatigue properties of HACS. HACSs formed at an HA-ADH/OCS ratio of 4:1 demonstrated high elastic recoverability after unloading in cyclic compression tests (Fig. 6i), indicating that the ECM analog-based hydrogel preserved the dynamic mechanical responses of healthy ECM and can withstand the frequent compression in IVD environment. Based on these findings, the HA-ADH/OCS ratio of 4:1 was ultimately selected on account of the optimized exosome delivery and mechanical performance.

Under IDD-like slightly acidic conditions, the Schiff base linker would be readily cleaved, causing gradual degradation of the hydrogel (Supplementary Fig. 15). Indeed, we have comparably investigated the degradation kinetics of HACS under pH 7.4 (physiological pH), pH 6.5 (mild IDD-like condition) and pH 5.5 (severe IDD-like conditions). The degradation rates of HACS hydrogels showed a general positive correlation with the acidity of the culture solution, which were 20%, 49%, and 69% after 14 days of incubation in phosphate-buffered saline (PBS) at pH 7.4, 6.5, and 5.5, respectively, ascribing to the to the cleavage of Schiff base linkages under acidic conditions (Fig. 6j). Similar trends were also observed for HACS incubated in other typical biomimetic buffer solutions including saline and DMEM/F12 (Supplementary Fig. 16). The microenvironment-responsive degradation of the HACS substrate may facilitate the complete elimination of the hydrogel fillers after completing IVD restoration for avoiding potential long-term health risks.

The as-synthesized HACS hydrogels were then deployed as loading matrices for CPP-miR-Exo (HACS@CPP-miR-Exo), which was achieved through a simple pre-mixing approach by adding CPP-miR-Exo into the ECM analog solutions before gelation (Fig. 6a). Confocal microscopy revealed efficient and homogenous encapsulation of CPP-miR-Exo in the hydrogel matrix (Fig. 7a, b). SEM analysis further confirmed the presence of abundant exosomes in

https://doi.org/10.1038/s41467-025-58447-5

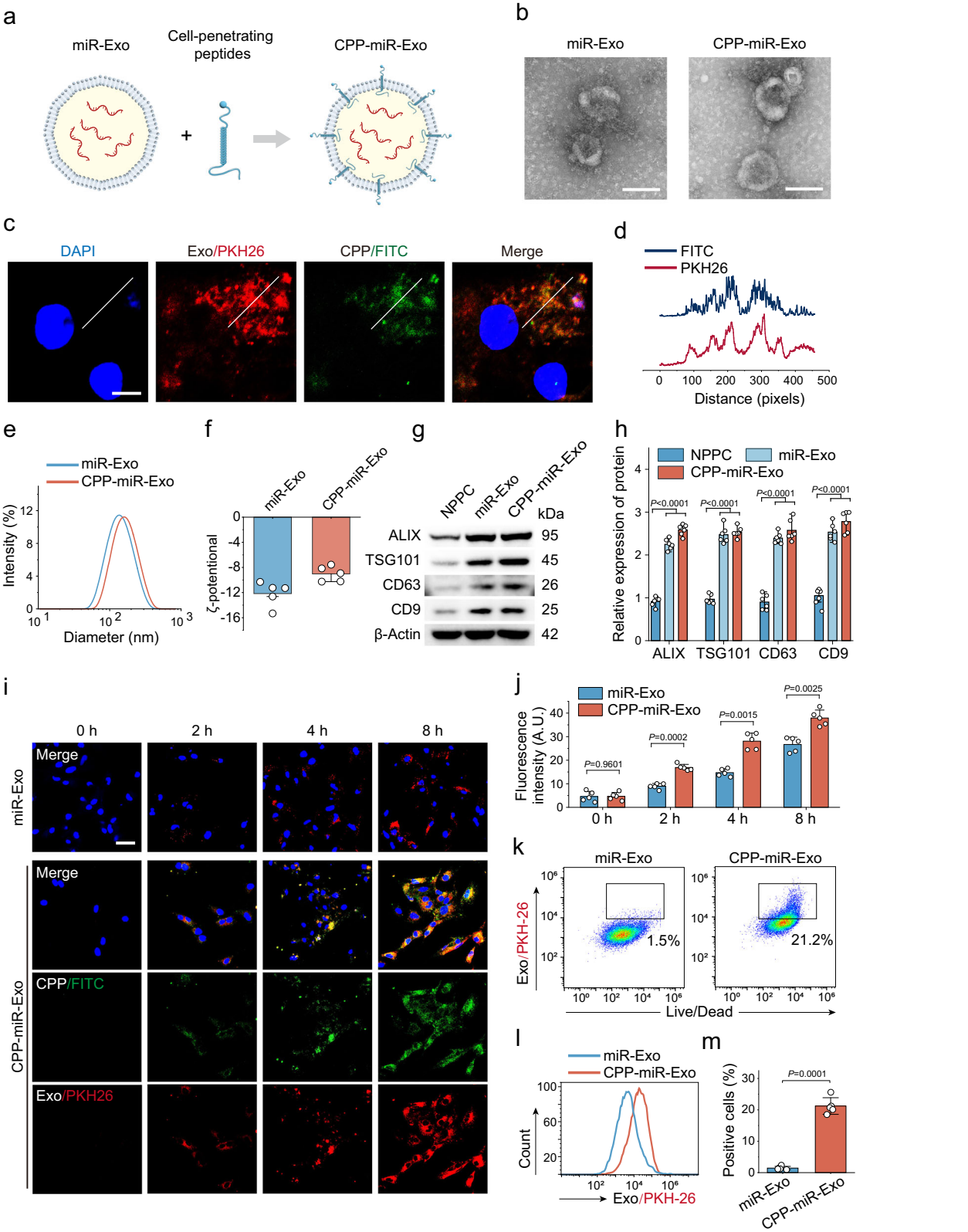

the HACS@CPP-miR-Exo samples, which maintained their characteristic spherical morphology. Contrastingly, no spherical nanostructures were observed in HACS samples (Fig. 7c). Moreover, the protein profiles of HACS@CPP-miR-Exo aligned with those of CPP-miR-Exo (Fig. 7d), suggesting the adequate preservation of exosomal proteins after encapsulation. We then investigated the release of CPP-miR-Exo from HACS@CPP-miR-Exo via fluorescence imaging. HACS@CPP-miR-Exo underwent gradual degradation upon incubation in PBS and released exosomes into solution environment through a period of 14 days (Fig. 7e, f). Furthermore, evaluation on two-dimensional (2D) and three-dimensional (3D) cell culture systems (Fig. 7h-n) showed that inoculation on HACS@CPP-miR-Exo matrix induced no obvious negative impact on the viability and proliferation of NPCs, accompanied with substantial uptake of

Fig. 5 | Engineering and characterization of CPP-miR-Exo. a Engineering procedures of CPP-miR-Exo. **b** Representative TEM images of miR-Exo and CPP-miR-Exo. Scale bars, 200 nm. **c** CLSM images illustrate the cellular uptake of CPP-miR-Exo in NPCs. miR-Exo and CPP were labeled with PKH26 and FITC, respectively. Scale bars, 10 μm. **d** Representative fluorescence intensity profiles of FITC compared with PKH26 in the radial direction of the white lines in (**c**). Size distribution (**e**) and ζ-potential (**f**) of miR-Exo and CPP-miR-Exo. $n = 5$ biologically independent samples for panel (**f**). Western blot bands (**g**) and quantitative analysis (**h**) showing the expression of exosome markers in miR-Exo and CPP-miR-Exo ($n = 6$ biologically independent samples). Fluorescence images (**i**) and quantitative analysis (**j**) demonstrating the time-dependent internalization of miR-Exo or CPP-miR-Exo at 50 μg/mL in NPCs ($n = 5$ biologically independent samples). Scale bar, 100 μm. Representative flow cytometric profiles (**k**–**l**) and quantitative analysis (**m**) of the uptake of miR-Exo in NPCs after 4 h of co-culture ($n = 5$ biologically independent samples). Comparisons were performed by two-tailed Student's t test in panels (**h**, **j** and **m**). Data are presented as means ± SD. $n = 3$ independent experiments for panels (**b**, **c**, **e**). NPPC nucleus pulposus progenitor cell, NPPC-Exo NPPC-derived exosome, miR-Exo miR-221-3p overexpressed NPPC-Exo CPP, cell-penetrating peptide, CPP-miR-Exo cell-penetrating peptide modified miR-Exo. Schematic illustrations were generated using BioRender (Wang, V., 2025; accessible at: https://BioRender.com/i62o243). Source data are provided as a Source Data file.

CPP-miR-Exo (Fig. 7g). Notably, the hydrogel-mediated exosome delivery to Erastin-conditioned ferroptotic NPCs potently attenuated intracellular ROS and ferrous ion levels thereof (Fig. 7o-q), immediately supporting its anti-ferroptosis potential. Furthermore, in vitro viability assays on NPCs demonstrated that OCS, HA-ADH, and HACS exhibited negligible cytotoxicity even at a high concentration of approximately 1 mg/mL (Supplementary Fig. 17). Collectively, these results indicate that the HACS@CPP-miR-Exo represents a robust in-situ CPP-miR-Exo delivery platform for the sustainable inhibition of ferroptosis in NPCs with optimal safety.

Evaluation of the exosome release profiles of HACS@CPP-miR-Exo in vivo

The sustained presence of the anti-ferroptosis exosomes in the NPs is crucial for enabling long-term protection against post-operative LDH. Herein, the exosome delivery performance of HACS@CPP-miR-Exo was first evaluated on rat models with caudal IVD discectomy and monitored the IDD progression after in situ injection of HACS@CPP-miR-Exo into the NP cavity (Fig. 8a). The CPP-miR-Exo was labeled with the fluorescent dye DID and the retention of the exosomes delivered to the IVD was observed through in vivo imaging (Fig. 8b). The results demonstrated that hydrogel matrices substantially enhanced the retention time of the engineered exosomes in the NP environment, for which strong DID fluorescence could still be observed on day 28 after a single administration (Fig. 8c). Furthermore, we also performed immunofluorescence staining of IVD sections in rats with HACS@CPP-miR-Exo treatment. Fluorescence observation of frozen sections indicated abundant FITC-labeled CPP and DID-labeled exosomes in the NPs at day 7 post-injection, of which the signals showed strong overlap and suggested efficient exosome release from the hydrogel substrate (Fig. 8d, e). Aggrecan immunofluorescence staining further confirmed that the released CPP-miR-Exos were internalized by a substantial number of NPCs (Fig. 8f, g). Taken together, these results demonstrated that HACS@CPP-miR-Exo could be gradually degraded in the NP cavity and release the therapeutic exosomes in a sustainable manner across a long period.

The biosafety of the biomimetic hydrogel was also comprehensively investigated in vivo using rat models. Following a single injection of HACS, free CPP-miR-Exo, or HACS@CPP-miR-Exo into the discs of rats from different experimental groups, no significant differences in body weight were observed (Supplementary Fig. 18a). Two months post-administration, the organ index values for the heart, liver, spleen, lungs, and kidneys were measured and showed no significant changes across all groups (Supplementary Fig. 18b). Meanwhile, there were no notable differences in the hepatic and renal functions among different groups (Supplementary Fig. 18c–j). Histological analysis of H&E-stained sections from the major organs also revealed no obvious pathological alterations in all groups (Supplementary Fig. 18k). These findings collectively demonstrate the biocompatibility of the HACS hydrogel, suggesting its safety for potential clinical applications.

HACS@CPP-miR-Exo reverses post-discectomy IDD

The efficacy of HACS@CPP-miR-Exo for treating post-discectomy rLDH and IDD was eventually evaluated in rat models of discectomy (Fig. 9a). Magnetic resonance imaging (MRI) showed that IDD rats treated with HACS@CPP-miR-Exo exhibited the greatest improvements in IVD height and NP volume compared with the model group, which was almost comparable to the IVD in healthy rats (Fig. 9b, c). In contrast, both HACS and CPP-miR-Exo treatments showed modest IVD recovery at varying degrees on account of the associated therapeutic benefits but were both inferior to the integral therapy. Safranine O-Fast Green staining of IVD sections from the treatment-free control group showed marked NP atrophy and fibrosis one month after discectomy, both of which are hallmark features of IDD (Fig. 9b). Notably, rats in the HACS@CPP-miR-Exo group showed the greatest increase in the disc height index (DHI) and water content of the degenerative IVDs with markedly reduced histological grade among all groups, indicating the effective reversal of post-discectomy disc degeneration thereof (Fig. 9c–e). Histological examination with H&E and Safranine O-Fast Green staining revealed that HACS@CPP-miR-Exo group showed the most pronounced NP restoration, with marked inhibition of NP shrinkage and fibrosis. To investigate the IVD rescue mechanism of the treatment in vivo, we performed immunohistochemical staining on extracted IVD samples. The results suggested that both the CPP-miR-Exo and HACS@CPP-miR-Exo groups showed upregulated GPX4 expression and inhibited ACSL4 expression in IVD tissues (Fig. 9f, g), suggesting that the CPP-miR-Exo contents are the major contributors to the inhibition of NPC-intrinsic ferroptosis for reversing disc regeneration. Notably, HACS@CPP-miR-Exo showed superior anti-ferroptosis efficacy than CPP-miR-Exo with higher ACSL4 inhibition and GPX4 promotion effects, supporting our hypothesis that HACS@CPP-miR-Exo could reverse post-discectomy IDD through improving the delivery efficacy of anti-ferroptotic CPP-miR-Exo. Moreover, HACS@CPP-miR-Exo treatment significantly decreased the cellular MDA and ferrous ion levels in NPCs (Fig. 9h, i), further validating our hypothesis that the HACS@CPP-miR-Exo treatment could inhibit NPC ferroptosis via the in-situ delivery of miR-221-3p-laden exosomes to facilitate IVD recovery.

Discussion

LDH is one of the common osteoarthrosis diseases due to IDD with terrible consequences including chronic pain and severe disability[49]. Endoscopic discectomy is an emerging surgical therapy for LDH treatment and gains increasing interest in the clinic practice on account of its immediate pressure alleviation, minimal invasiveness and high cost-effectiveness[2,50]. However, recent studies have indicated that the persistent degenerative phenotypes of NPCs and the discectomy-induced stress significantly contribute to the pathogenesis of rLDH, which would markedly impair the efficacy of discectomy and often requires revision surgery[3,4]. Previous studies have highlighted the critical role of ferroptosis in driving NPC degeneration and promoting rLDH[5,6,51], emerging as a promising therapeutic target for

https://doi.org/10.1038/s41467-025-58447-5

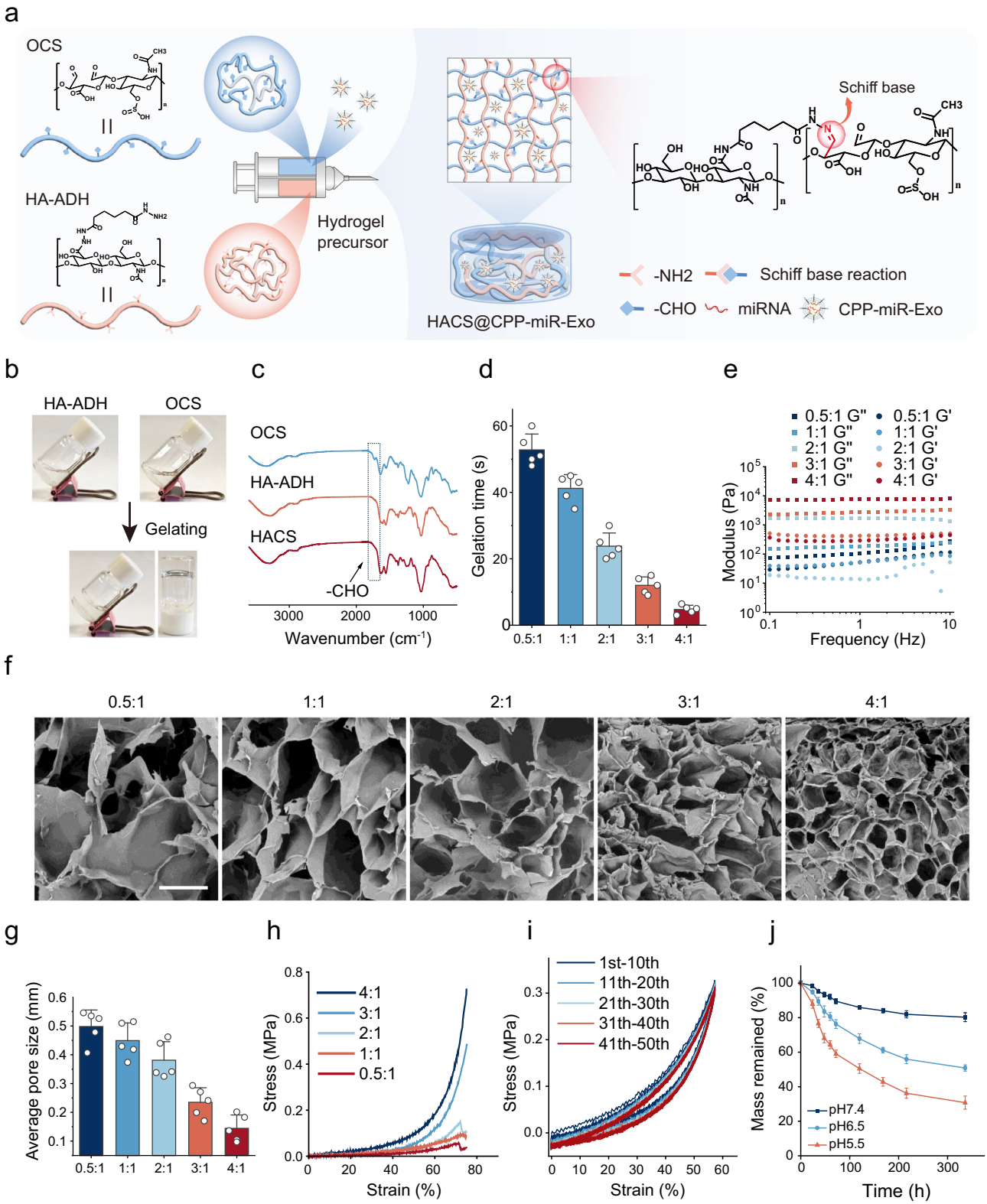

Fig. 6 | The preparation and characterization of HACS@CPP-miR-Exo. **a** Preparation of HACS@CPP-miR-Exo. **b** Digital photos showing the formation of HACS by mixing HA-ADH and OCS solution. **c** FTIR spectra of OCS, HA-ADH, and HACS. **d** The gelation time of HACS at various volume ratios of HA-ADH to OCS ($n = 5$ biologically independent samples). **e** The storage modulus (G′) and loss modulus (G″) of HACS under different precursor ratios. The typical SEM images after freeze-drying (**f**) and quantification of pore size (**g**) of HACS under different precursor ratios ($n = 5$ biologically independent samples). Scale bar, 500 μm. Young's modulus (**h**) and typical compression cycle curves (**i**) of HACS under different precursor ratios. **j** The degradation behavior of HACS under different pH conditions ($n = 3$ biologically independent samples). Data are expressed as means ± SD. $n = 5$ independent experiments for panel (**f**). OCS oxidized chondroitin sulfate, HA hyaluronic acid, HA-ADH adipic acid dihydrazide-modified HA, HACS ECM-mimetic hydrogel; CPP-miR-Exo cell-penetrating peptide modified miR-Exo. Schematic illustrations were generated using BioRender (Wang, V., 2025; accessible at: https://BioRender.com/i62o243). Source data are provided as a Source Data file.

https://doi.org/10.1038/s41467-025-58447-5

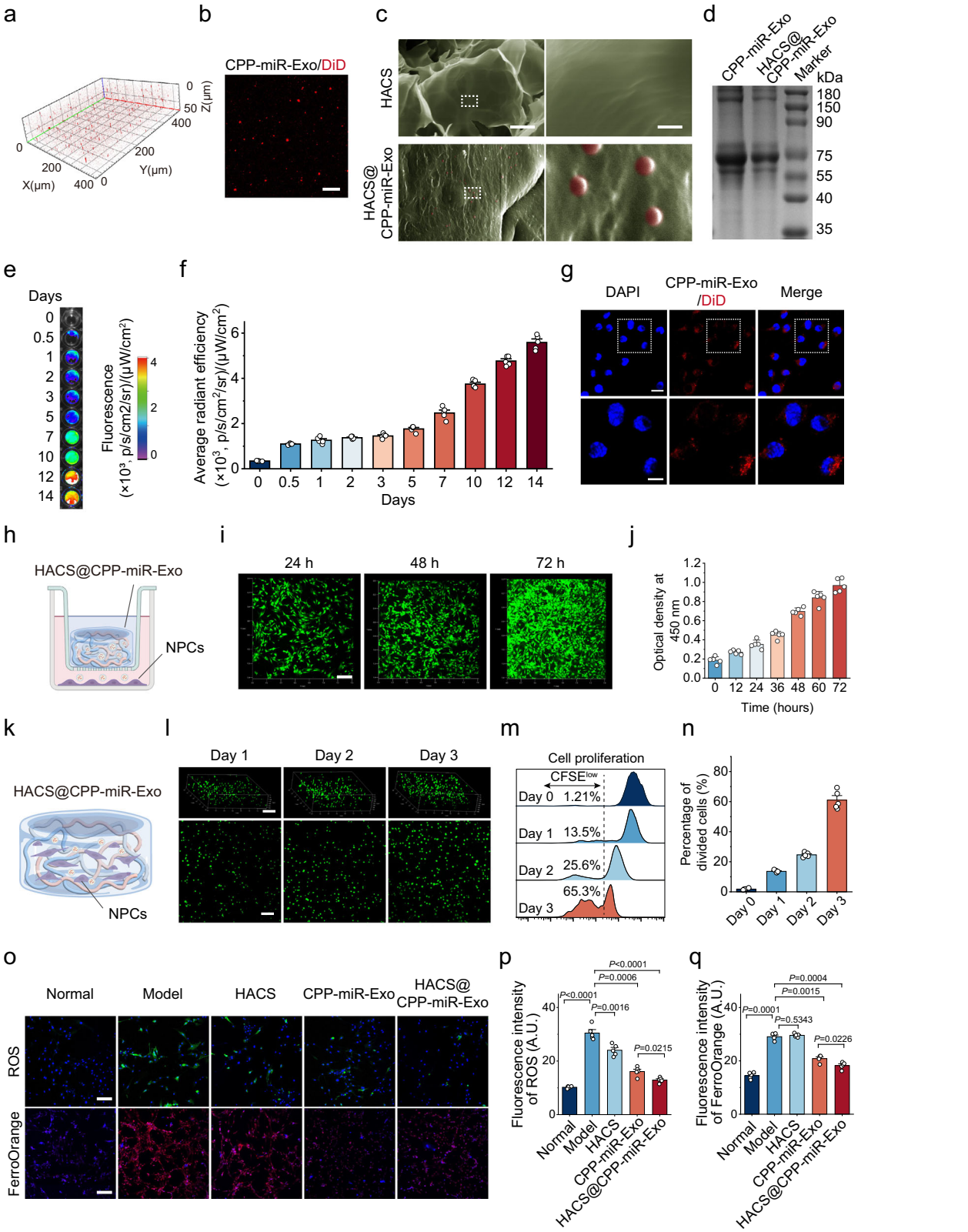

preventing rLDH and reversing the degeneration post-discectomy. However, reports on the development of anti-ferroptosis therapeutics for the treatment of degenerative IVD are still rare. While post-discectomy IDD is a complex indication involving multiple cell death programs including ferroptosis, apoptosis and pyroptosis, here we identified that ferroptosis of NPCs is a major contributor to its onset and progression through NP degeneration rescue experiment with various cell death inhibitors and RNA sequencing analysis. Interestingly, we discovered that NPPCs could imprint their ferroptosis resistance to surrounding NPCs via exosome-dependent intercellular communication, which may deliver miR-221-3p to activate the NPC-intrinsic STAT1 signaling in an endocrine-like manner, substantiating the application of NPPC-derived exosomes as a biocompatible modality for reversing the degeneration of ferroptotic NPCs.

Fig. 7 | In vitro biological effects of HACS@CPP-miR-Exo. a, **b** CLSM images of HACS@CPP-miR-Exo. **a** Three-dimensional reconstruction of DiD-labeled miR-Exo in HACS@CPP-miR-Exo. **b** Representative fluorescence image showing DiD-labeled CPP-miR-Exo in HACS@CPP-miR-Exo. Scale bar, 1 μm. **c** Representative SEM images of HACS@CPP-miR-Exo hydrogel. The pseudo-red patterns indicate miR-Exo. Scale bar, 2 μm (left) and 200 nm (right). **d** SDS-PAGE analysis of CPP-miR-Exo and HACS@CPP-miR-Exo after Coomassie Blue staining. $n = 3$ biologically independent samples for panels (**a**–**d**). Luminescent images (**e**) and corresponding quantitative data (**f**) on miR-Exo release from the HACS@CPP-miR-Exo hydrogel ($n = 5$ biologically independent samples). miR-Exo was labeled with the cell membrane dye DiD. **g** Fluorescence images showing the cellular uptake of CPP-miR-Exo released from HACS@CPP-miR-Exo in NPCs 4 h after incubation, demonstrated by a transwell assay. Lower panels are the magnified fluorescence images in marked regions. Scale bars, 100 μm (upper) and 20 μm (lower). **h** A schematic diagram illustrates the transwell co-culture system of NPCs with HACS@CPP-miR-Exo. **i** Observation of CFSE labeled NPCs under a transwell co-culture assay with HACS. Scale bar, 200 μm. **j** Viability of NPCs cultured with HACS in the transwell co-culture systems examined by CCK-8 assays ($n = 5$ biologically independent samples). **k** A schematic diagram illustrates the 3D co-culture system of NPCs with HACS. **l** Observation of CFSE labeled NPCs under a 3D co-culture system with HACS. Scale bar, 250 μm. Flow cytometric profiles (**m**) and quantification (**n**) shows the cell proliferation of NPCs under a 3D co-culture system with HACS ($n = 5$ biologically independent samples). Representative fluorescence images (**o**) and quantification of ROS (**p**) and FerroOrange (**q**) probe staining showing the levels of cellular ROS and ferrous ion in NPCs of different groups ($n = 5$ biologically independent samples). Scale bar, 200 μm. Comparisons were performed by two-tailed Student's t test in panels (**p**, **q**). Data are presented as means ± SD. HACS ECM-mimetic hydrogel, CPP-miR-Exo cell-penetrating peptide modified miR-Exo, NPCs nucleus pulposus cells. DiD, 1,1′-dioctadecyl-3,3,3′,3′-tetramethylindodicarbocyanine,4-chlorobenzenesulfonate salt, a far-red plasma membrane fluorescent probe. Schematic illustrations were generated using BioRender (Wang, V., 2025; accessible at: https://BioRender.com/i62o243). Source data are provided as a Source Data file.

Despite their significant application potential, the clinical translation of exosome therapeutics remains challenging due to low productivity and insufficient expression of therapeutically relevant exosomal contents[52–54]. To overcome these challenges, we further developed a multi-level synthesis strategy for the engineering of NPPC-derived exosomes, aiming to enhance their therapeutic efficacy under clinically relevant conditions. Specifically, the adenovirus-enabled genetic engineering of NPPCs allowed the generation of exosomes with significantly higher miR-221-3p loading, of which the miR-221-3p levels were forty times higher than those transfection-free control groups, suggesting greater anti-ferroptosis capacity for the degenerative NPCs. Meanwhile, to facilitate the exosome homing to NPCs in the complex NP microenvironment, the NPPC-derived exosomes were further modified with CPP ligands via non-invasive cholesterol-dependent membrane insertion mechanisms, which could substantially enhance the exosome uptake by NPCs without impairing their anti-ferroptosis functions. The tailoring of NPPC-derived exosomes substantially enhanced the rescue effect on ferroptosis-affected degenerative NPCs with optimal safety.

On the other hand, it is well-established that IDD is a chronic condition and the successful reversal of its degeneration symptoms requires the sustained presence of the NPPC-derived exosomes in the NP microenvironment. Indeed, clinical data collectively demonstrate that the translation of exosome-based therapeutics is profoundly impeded by their rapid clearance after systemic and local administration, leading to insufficient accumulation in desired site of action[54,55]. Interestingly, hydrogels have emerged as a promising modality for in-situ exosome delivery on account of their intrinsic biocompatibility, tailorable biological functions and versatile drug delivery capability[56,57]. There is already ample evidence that hydrogels could not only enable the non-invasive incorporation of therapeutic active exosomes through physical encapsulation but also release them in a spontaneous or triggerable manner, affording additional opportunities for the treatment of a broad spectrum of degenerative and chronic diseases[58–60]. For this purpose, we developed an injectable HACS@CPP-miR-Exo hydrogel system based on biocompatible ECM analogs for the non-invasive incorporation and in situ delivery of engineered exosomes to post-discectomy NPs. The HACS@CPP-miR-Exos were directly injected into the post-discectomy cavity and achieved sustained exosome release for up to 28 days, leading to marked inhibition of the ferroptosis programs in NPCs to reverse their degenerative phenotype. Moreover, owing to the structural and chemical resemblance of the HACS hydrogels to natural ECM in NP tissues, the HACS@CPP-miR-Exo filler maintained the dynamic mechanical properties of healthy ECMs, which may facilitate the post-operational recovery of defective IVDs. These merits supported the potential application of the HACS@CPP-miR-Exo hydrogel as an anti-ferroptosis NP filler for post-discectomy care of IVDs.

In terms of the translational potential of the biomimetic hydrogels, we have proposed several potential strategies that may improve their upscalability and utility for clinical applications, focusing on (1) large-scale preparation of high quality miR-Exos and (2) optimizing the efficacy, safety and patient compliance of NP-targeted hydrogel administration. Specifically, the tremendous progress in ex vivo expansion technology of stem cells in recent years offers promises to overcome the potential shortage of NPPC-derived exosomes while ensuring exosome quality and consistency[61–63]. Meanwhile, on account of the good injectability, biocompatibility and biodegradability of the biomimetic hydrogels, they can be facilely administered either through direct intraoperative injection at the surgical site or via post-operative percutaneous injection, thus minimizing the complexity of the treatment procedures while enhancing patient compliance. We envision that these technologies could substantially facilitate the up-scale production and translation of the biomimetic hydrogel for post-discectomy IDD treatment on real-life patients.

In summary, this study reports an innovative hydrogel-based strategy to prevent post discectomy rLDH and IDD by harnessing the anti-ferroptosis activity of NPPC-derived exosomes, opening a different avenue for disc herniation treatment in the clinics.

Methods

Ethical statement

All experimental procedures involving animals were conducted in strict compliance with both institutional and national ethical guidelines. This study was performed in accordance with the National Institutes of Health Guide for the Care and Use of Laboratory Animals (8th edition, 2011) and was formally reviewed and approved by the Institutional Animal Care and Use Committee of Third Military Medical University (Approval ID: AMUWEC20223882; Chongqing, China).

Materials

Hyaluronic acid, chondroitin sulfate, adipic acid dihydrazide, 4-(bromomethyl) phenylboronic acid, 1-(3-dimethylamino propyl)-3-ethyl carbodiimide hydrochloride (EDC), N-hydroxy succinimide (NHS), and sodium periodate were purchased from Aladdin (U.S.A.). Penicillin and streptomycin, 2′,7′-dichlorofluorescin diacetate (DCFH-DA), 4′6-Diamidino-2-phenylindole (DAPI), RIPA lysis buffer (P0013), BCA protein assay kit (P0012S), Lipid Peroxidation MDA Assay Kit (S0131S), DiD dyes (C1039), Hoechst (C1022), HRP-conjugated goat anti-rabbit IgG (1:3000, A0208), HRP-conjugated goat anti-mouse IgG (1:3000, A0216), Alexa Fluor 555-labeled donkey anti-rabbit IgG (1:500, A0453), and Alexa Fluor 488-labeled Goat anti-mouse IgG (1:500, A0428) antibody were purchased from Beyotime Biotechnology (Shanghai,

https://doi.org/10.1038/s41467-025-58447-5

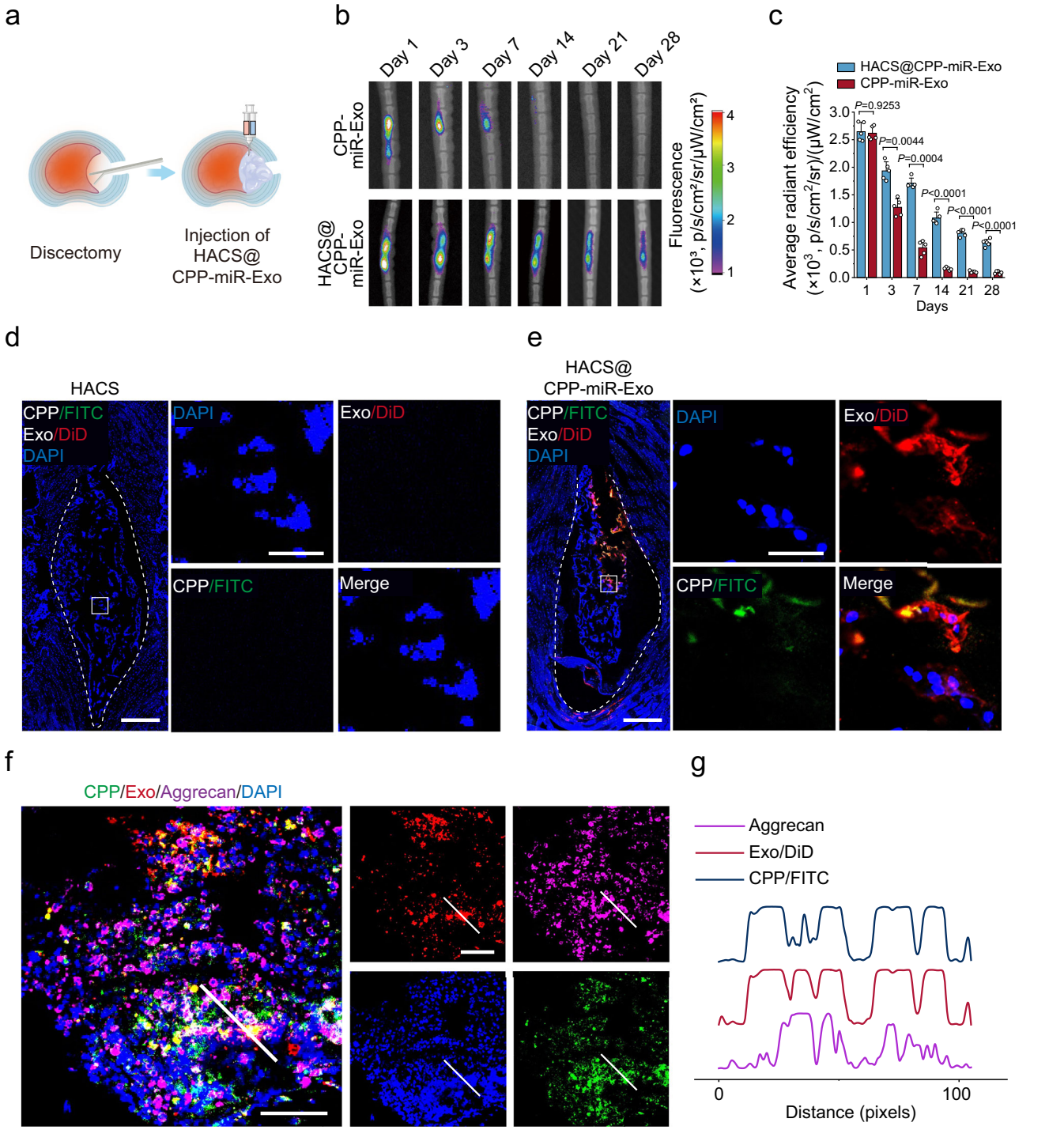

Fig. 8 | In vivo miR-Exo delivery using HACS@CPP-miR-Exo. a A diagram illustrating the discectomy of the rat caudal IVD and the administration of HACS@CPP-miR-Exo. Real-time in vivo images (**b**) and quantitative data (**c**) demonstrating the in-situ retention of CPP-miR-Exo in rat caudal IVDs after the injection of CPP-miR-Exo or HACS@CPP-miR-Exo ($n = 5$ biologically independent samples). **d**, **e** Fluorescence images of IVD cryosections displaying the distribution of CPP-miR-Exo 48 h post-injection. The nuclei were stained with DAPI. Scale bar, 500 μm (left) and 50 μm (right). **f** Representative immunofluorescence images revealing the co-localization of CPP-miR-Exo with aggrecan$^+$ NPCs in IVD cryosections at 48 h post-injection. Scale bar, 50 μm (left) and 50 μm (right). **g** Representative fluorescence intensity profiles of FITC (CPP), DiD (exosomes) and AF-555 (Aggrecan) in the radial direction of the white lines in (**f**). $n = 3$ independent experiments for panels (**d**–**g**). Comparisons were performed by two-tailed Student's t test in panel (**c**). Data are presented as means ± SD. HACS ECM-mimetic hydrogel, CPP-miR-Exo cell-penetrating peptide modified miR-Exo, DiD, a far-red plasma membrane fluorescent probe. Schematic illustrations were generated using BioRender (Wang, V., 2025; accessible at: https://BioRender.com/i62o243). Source data are provided as a Source Data file.

China). Western HRP substrate (WBKLS0100) and 0.45 μm PVDF transfer membrane (IEVH00005) were purchased from Millipore (U.S.A.). Total RNA extract reagent (RNAiso Plus, 9108) and small RNA extract reagent (RNAiso for Small RNA, 9753 A) was provided from TaKaRa (Japan). Tris-HCl SDS-PAGE at 7.5% or 10% (TGX Stain-Free™ FastCast™ Acrylamide Kit) was purchased from Bio-Rad (U.S.A.). Fetal bovine serum (FBS) was purchased from Zhejiang Tianhang Biotechnology Co. Ltd (Zhejiang, China). DMEM/F12 medium was

https://doi.org/10.1038/s41467-025-58447-5

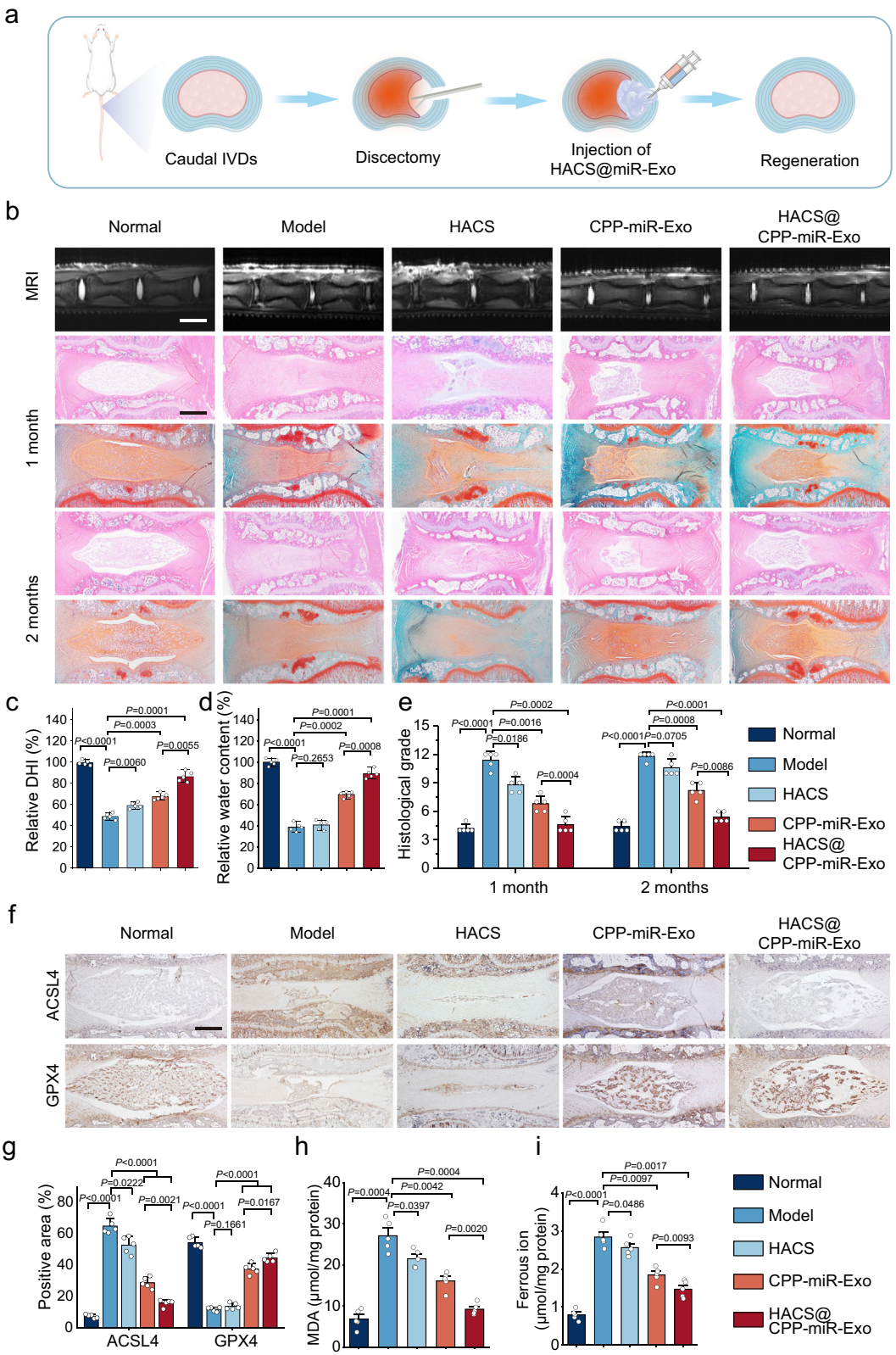

obtained from Gibco (U.S.A.). Rabbit anti-COL2 (1:500, 28459-1-AP), anti-Aggrecan (13880-1-AP), anti-CD90 (1:200, 27178-1-AP), anti-CD44 (1:200, 15675-1-AP), anti-CD105 (1:200, 10862-1-AP), anti-GPX4 (1:500, 30388-1-AP), anti-ACSL4 (1:1000, 22401-1-AP), anti-ALIX (1:500, 12422-1-AP), anti-TSG101 (1:500, 28283-1-AP), anti-CD63(1:500, 25682-1-AP), anti-CD9 (1:500, 20597-1-AP), anti-STAT1 (10144-2-AP), anti-SLC7A11 (26864-1-AP), and anti-β-Actin (1:1000, 81115-1-RR) antibodies were purchased from Proteintech (Hubei, China). Rabbit anti-pSTAT1 (ET1611-20) antibody was obtained from HUABIO (Hangzhou, China). Rabbit anti-IRF8 antibody (98344S) was purchased from CST (U.S.A.). Erastin (HY-15763), Fludarabine (HY-B0069), Ferrostatin-1(HY-100579), Deferoxamine (HY-B1625), ZVAD-FMK (HY-16658B), Necrosulfonamide (HY-100573), Cell Counting Kit-8 (HY-K0301), RT Master Mix for qPCR II (gDNA digester plus) (HY-K0511A), and SYBR Green

Fig. 9 | HACS@CPP-miR-Exo therapy promotes IVD restoration following discectomy. a Schematic representation illustrating IVD discectomy in rats and the associated treatment protocols. **b** In vivo radiological and histological assessments. MRI scans of rat caudal IVDs were conducted 2 weeks post-discectomy. H&E staining and Safranin-O/Fast Green staining of IVD sections were performed at 1- or 2-months post-discectomy. Scale bar: 5 mm (up) and 500 μm (down). **c** Quantitative analysis of DHI after various treatments according to the MRI scanning data ($n = 5$ independent rats). **d** Quantitative analysis of disc water content after various treatments according to the MRI scanning data ($n = 5$ independent rats). **e** Histological grades of the IVD after different treatment ($n = 5$ independent rats). Representative immunohistochemical staining images (**f**) and quantification (**g**) of ACSL4 and GPX4 in IVD sections ($n = 5$ independent rats). Scale bar: 500 μm. **h**–**i** Assessment of MDA and ferrous ion levels in IVDs across different groups ($n = 5$ independent rats). Comparisons were performed by two-tailed Student's t test in panels (**c**, **d**, **e**, **g**, **h** and **i**). Data are presented as means ± SD. $n = 5$ independent rats for panels (**b**, **f**). IVD intervertebral disc, HACS ECM-mimetic hydrogel, CPP-miR-Exo cell-penetrating peptide modified miR-Exo, DHI disc height index, ACSL4 acyl-coenzyme A synthetase long-chain family member 4, GPX4 Glutathione Peroxidase 4, MDA malondialdehyde. Schematic illustrations were generated using BioRender (Wang, V., 2025; accessible at: https://BioRender.com/i62o243). Source data are provided as a Source Data file.

qPCR Master Mix (HY-K0501A) were purchased from MCE (U.S.A.). miRNA First Strand cDNA Synthesis kit (Stem-loop Method, B532453) was purchased from Sangon Biotech (Shanghai, China). Safranine O-Fast Green Staining Kit (G1371) and PKH26 Cell Membrane Staining Kit (D0030) were provided by Solarbio (Beijing, China). BODIPY™ 581/591 C11 fluorescent probe (D3861) was purchased from Invitrogen (U.S.A.). Intracellular Iron Measurement FerroOrange indicator (F374) was purchased from Dojindo (Japan). Mesenchymal Stem Cells (Rat) Surface Marker Detection Kit (RAXMX-09011) were purchased from Cyagen (U.S.A.). Iron Assay Kit (ab83366) was purchased from Abcam (U.K.). DAB Chromogenic Kit (ZLI-9018) and Goat anti-mouse/rabbit IgG polymer (PV-6000) were purchased from ZSGB-BIO (Beijing, China). CFSE Cell Division Tracker Kit (423801) was purchased from BioLegend (U.S.A.). EDTA decalcification solution was purchased from BOSTER (Wuhan, China). IL-1β ELISA kit (MM-0047R1) was purchased from Meimian (Jiangsu, China).

Reanalysis of the GEO database

To investigate the contributing factors of post-discectomy rLDH and IDD degeneration, we selected GSE70362 dataset in the GEO database of human IVDs. According to the Thompson grade system[16], we regrouped the samples of the GSE70362 into the control (grade I and II) and IDD (grade IV and V) subsets. Grade I NP tissues are gel-like with neatly arranged AF structures, presenting thick and uniform cartilage endplates (CEP) and regular vertebral body margin. Grade II NP tissues are characterized by emerging white fibrous tissues at the edge of the NPs, with mucin-like substances between the layers of the AF, irregular CEP thickness and protrusion at the vertebral body margin. Based on clinical standards, Grade I and Grade II samples are generally recognized as healthy IVDs and consolidated into a single group named "Control". For Grade III samples, obvious sclerotic fibrous tissues are located within the NP, the boundary between the AF and NP is unclear with abundant mucin-like substance in the AF, focal defects are visible in the CEP, and scattered osteophytes are present at the vertebral body margin. For grade IV samples, horizontal fissures parallel to the CEP are observed within the NP, radial or annular ruptures are found in the AF, focal sclerosis is present beneath the cartilage of the CEP, and vertebral osteophytes are less than 2 mm in size. On account of these pathological traits, Grade III and Grade IV samples are classified as degenerative types and consolidated into a single group named "IDD".

Animals and surgical procedures

Newborn and adult Sprague-Dawley rats of both sexes were of Specific Pathogen Free (SPF)-grade and obtained from the Experimental Animal Center of Third Military Medical University (Army Medical University, Chongqing, China). Animals were housed under controlled environmental conditions (25 ± 2°C, 50 ± 10% humidity, 12/12 h light/dark cycle). After being randomized to different groups, the rats were first anesthetized with 1% pentobarbital sodium (4 mL/kg) through intraperitoneal injections before the surgical procedures. After anesthesia, the tails of rats were sterilized, followed by a longitudinal median incision made on the tail skin to expose the IVD located at coccyx vertebrae. The IVD was punctured vertically with a microscalpel and the NP was excised partially in a microscopic forceps.

Isolation of nucleus pulposus progenitor cells (NPPC) from newborn rats

NPPCs were harvested from the IVD of newborn rats and cultured in DMEM/F12 medium[64]. Briefly, NP tissues of newborn rats were harvested and digested comprehensively by collagenase II (0.1–0.2%) in DMEM/F12 medium at 37 °C for 30 min. Then the cells were filtered using a 70 μm cell strainer and washed with PBS for three times. Subsequently, NPPCs were resuspended and cultured in DMEM/F12 medium (10% FBS, 1% penicillin/streptomycin).

Isolation of nucleus pulposus cells (NPC) from IVD of adult rats: NP tissues of adult rats were digested by collagenase II (0.1–0.2%) in DMEM/F12 medium at 37 °C for 30 min. Then the cells were filtered using a 70 μm cell strainer and washed with PBS for three times. Subsequently, NPCs were resuspended and cultured in DMEM/F12 medium (10% FBS, 1% penicillin/streptomycin).

Histological assessments and immunohistochemical analyses: Rat IVDs were harvested and fixed in 4% PFA, followed with decalcification in 10% EDTA. Then the samples were embedded in paraffin and prepared for coronal sections (4 μm) using a rotary microtome (Leica 149AUTO00C1, UK). The procedures were conducted according to the manufacturer's instructions for H&E and Safranine O-Fast Green staining. For Immunohistochemical assays, sections were incubated with primary antibodies, followed by incubation with corresponding HRP-conjugated secondary antibodies. Hematoxylin was used to counterstain nuclei. The immunohistochemical outcomes were visualized with diaminobenzidine (DAB) reaction. Finally, the images were observed under an upright microscope (BX53, Olympus, Japan) and quantified with ImageJ analysis (V1.8, NIH). All experiments were repeated three times independently.

Immunofluorescence analysis

The frozen sections or cell adherent coverslips were incubated with primary antibodies, followed by incubation with fluorescence-conjugated secondary antibodies. DAPI was used to counterstain nuclei. Immunofluorescence was visualized using a Zeiss LSM880 confocal microscope, and images were acquired using the LSM software (Zeiss, UK). The images were quantified with ImageJ analysis (V1.8, NIH). All experiments were repeated three times independently.

Flow cytometry analysis

Flow cytometric analysis was conducted using a Gallios flow cytometer (Beckman Coulter, CA, USA). Following PBS (pH 7.4) washing, cells were adjusted to a density of 1×10^6 cells/mL in staining buffer. For direct surface marker detection, cells were incubated with fluorochrome-conjugated primary antibodies at 4 °C for 30 min under light-protected conditions. Indirect immunostaining involved sequential incubations with unlabeled primary antibodies followed by species-matched fluorochrome-conjugated secondary antibodies. All antibody incubations were separated by three washes with ice-cold PBS (300 × g, 5 min). Finally, cells were resuspended in 500 μL PBS and

processed using standardized acquisition parameters. Data analysis was performed using FlowJo v10.8.1. All experiments were repeated three times independently. Comprehensive gating strategies for each flow cytometric analysis are presented in Supplementary Fig. 19 to facilitate data interpretation and experimental replication.

Cell culture

NPCs and NPPCs were cultured in DMEM/F12 medium, supplemented with 10% FBS and 1% penicillin-streptomycin, and incubated in a humidified atmosphere of 5% CO_2 at 37 °C. To induce ferroptosis, NPCs were incubated with Erastin at 0.1–5 μM for 48 h. for exosomes administration, NPPC-Exo were added into cell mediums at a concentration of 50 μg/mL. HEK293T cells were purchased from Procell (Wuhan, China), and were cultured in DMEM medium with 10% FBS and 1% penicillin-streptomycin.

Extraction and identification of exosomes

The NPPCs were washed twice with DPBS before being cultured in DMEM/F12 supplemented with exosome-depleted FBS. After a 2-day incubation period, exosomes were isolated from the collected supernatant using ultracentrifugation[55]. Briefly, the supernatant was initially centrifuged at 300 × *g* for 10 min to remove suspension cells, followed by a second centrifugation at 2000 × *g* for 10 min to remove dead cells. After that, cell debris was removed by a centrifugation at 10,000 × *g* for 10 min. Subsequently, the supernatant was subjected to ultracentrifugation at 100,000 × *g* for 70 min to obtain exosomes. The exosomes were then resuspended in PBS, filtered with a 0.22 μm filter, and centrifuged at 100,000 × *g* for 70 min. Finally, the exosomes were resuspended in 200 μL DPBS for downstream analysis.

Four methods were used to evaluate the characteristics of NPPC-Exo: nanoparticle tracking analysis (NTA), transmission electron microscopy (TEM), and western blot. The size distribution profiles and zeta-potential values of exosomes were analyzed using a Malvern Zetasizer NanoZS instrument for NTA. The morphology of NPPC-Exo was examined by TEM using a TECNAI-10 microscope (Philips, Netherlands) at an acceleration voltage of 80 kV. The experimental procedure for western blot was performed following the detailed description provided in the subsequent "Western blot analysis" section of this article.

TEM observation of NPCs

To prepare ultrathin sections for TEM, NPCs were centrifuged and collected. Then, the cell clumps were fixed with 2.5% glutaraldehyde, postfixed with 1% osmium, and embedded in resin and cut into 50-nm thick sections. TEM images were visualized and acquired using a Zeiss LIBRA 200 electron microscope.

Quantitative real-time polymerase chain reaction (qPCR) analysis

The total RNA of NP tissues from caudal IVD of rats was isolated following the manufacturer's instructions. Complementary DNA (cDNA) was acquired by reverse transcription experiments. First strand cDNA of miRNA was synthesized by stem-loop method. qPCR was performed with a SYBR dye in a CFX96 Touch Real-Time PCR Detection System (Bio-rad, U.S.A.). The primer sequences are listed in Supplementary Table 1.

miRNA sequencing analysis of exosomes

Total RNAs were isolated using the Total Exosome RNA Isolation Kit (Thermo Scientific) and miRNA sequencing was conducted by LC-Bio Technology Co., Ltd. (Hangzhou, China). The quality and quantity of total RNA were assessed using a Bioanalyzer 2100 (Agilent) with an RIN number >7.0. Small RNA libraries were prepared from approximately 1 μg of total RNA according to the TruSeq Small RNA Sample Prep Kits (Illumina) protocol. Single-end sequencing of 50 bp was performed on an Illumina HiSeq 2500. Raw reads were processed using an in-house program, ACGT101-miR (LC-Bio Technology), which removed adapter dimers, junk, low complexity, common RNA families (rRNA, tRNA, snRNA, snoRNA), and repeats. Unique sequences with lengths ranging from 18-26 nucleotides were mapped to specific species precursors in miRBase 22.0 using BLAST search to identify known miRNAs and previously uncharacterized 3p- and 5p-derived miRNAs. The alignment allowed for length variation at both 3′ and 5′ ends and one mismatch inside the sequence. Unique sequences mapping to mature miRNAs in hairpin arms of specific species were identified as known miRNAs. Unique sequences mapping to the other arm of the known specific species precursor hairpin, opposite to the annotated mature miRNA-containing arm, were considered newly identified 5p- or 3p-derived miRNA candidates.

RNA-sequencing (RNA-seq) analysis

Total RNA from NPCs was isolated using a TRIzol reagent (Invitrogen, U.S.A.). Then, the total RNA was quantified using NanoDrop ND-1000 (NanoDrop, U.S.A.) and assessed with a Bioanalyzer 2100 (Agilent, U.S.A.) with RIN > 7.0. The poly (A) RNA was purified from 1 μg total RNA using Dynabeads Oligo (25-61005, Thermo Fisher, U.S.A.) and fragmented using Magnesium RNA Fragmentation Module (NEB, cat.e6150, U.S.A.). cDNA was obtained by SuperScript™ II Reverse Transcriptase (Invitrogen, Cat. 1896649, U.S.A.). Then, the final cDNA library with an average insert size of 300 ± 50 bp was created. After that, 2×150 bp paired-end sequencing (PE150) on an Illumina Novaseq™ 6000 (LC-Bio Technology Co., Ltd., Hangzhou, China) was performed following the vendor's recommended protocol. The significant DEGs were filtered with thresholds of a $|\log_2(\text{fold change, FC})| > 2$ and P value < 0.05 using the R package DESeq2. Gene Ontology (GO) and Kyoto Encyclopedia of Genes and Genomes (KEGG) enrichment analyses of the DEGs were performed using the OmicStudio tools at https://www.omicstudio.cn.

Western blot analysis

Tissues or cells were collected and homogenized in ice-cold RIPA lysis buffer. Samples were then centrifuged at 12,000 × *g* for 20 min at 4°C, and the supernatant was acquired. Subsequently, 30 μg total proteins from each sample were loaded to 7.5% Tris-HCI SDS-PAGE and transferred onto 0.45 μm PVDF membranes. The membrane was incubated with the primary antibodies, followed by incubation with anti-HRP-conjugated secondary antibodies. The target protein bands were visualized by western HRP substrate and quantified using the ImageJ analysis (V1.8, NIH). Relative protein levels were normalized to the α-actin level on the same blot. Uncropped scans of WB bands in the supplementary information were shown in the Source Data file and Supplementary Fig. 20.

Dual luciferase reporter activity assay

The dual luciferase assay was conducted following established protocols (Promega, Madison, USA). The luciferase gene was inserted downstream of either the wild-type or mutant region of *Irf8* and co-transfected into HEK293T cells along with pmirGLO and a control vector. After 48 h, the cells were lysed, and the activity of firefly luciferase was assessed using the Dual-Luciferase® Reporter Assay System (Promega). The results were normalized to the internal reference of Renilla luciferase.

MDA and ferrous ion assays

NP tissues were collected and homogenized in ice-cold DPBS. Samples were then centrifuged at 12,000 × *g* for 20 min at 4 °C, and the supernatant was acquired. The MDA amount was evaluated using the MDA Assay Kit standardized. The ferrous ion amount was monitored using Iron Assay Kit.

Intracellular Fe^{2+}, ROS, and lipid peroxidation (LPO) assays

After removing the mediums, cells were incubated with FerroOrange (1 μM), DCFH-DA (10 μM), and BODIPY 581/591 Cll (5 μM) at 37 °C for 30 min. Subsequently, cells were washed with PBS and observed by confocal microscope (Zeiss LSM880, Germany). Moreover, cells were trypsinized and analyzed by flow cytometry (Beckman Gallios, U.S.A.).

Construction and infection of Adenovirus (AdV) for miR-221-3p overexpression

The AdV for miR-221-3p overexpression were provided from Genechem (Shanghai, China). The NPPCs were infected with AdV to obtain cells with overexpressed miR-221-3p, and thereby we acquired miR-221-3p overexpressed NPPC-Exo.

Synthesis and exosomal integration of CPP ligands

The CPP ligands were synthesized via a Michael addition reaction. Specifically, 30 mg of cholesterol-PEG2000-Maleimide was dissolved in 1 mL of DMF. Subsequently, the FITC-conjugated TAT peptide was added. The reaction mixture reacted for 12 h at room temperature and then transferred to a dialysis bag (molecular weight cut-off 3500 Da) and dialyzed in pure water for 24 h. The dialysate was collected and freeze-dried to obtain the desired product.

To modify the exosomes with CPP ligands, 500 μg of exosomes were added to 100 μL of 1 mg/mL CPP solution. The mixture was incubated at 25 °C and 250 rpm for 3 h, followed by standing at 4 °C for 24 h. The resulting engineered exosomes conjugated with CPP peptides were filtered and washed using a 100 kDa ultrafiltration unit.

Synthesis and characterization of HACS hydrogel

The synthesis of oxidized chondroitin sulfate (OCS) was performed as follows: 1 g of chondroitin sulfate was dissolved in 100 mL of distilled water, and 0.7 g of sodium periodate was added. The mixture was stirred for 48 h in the absence of light. Thereafter, 1 mL of ethylene glycol was added, and the mixture was further stirred for 30 min. The resulting mixture was transferred into a dialysis bag (MWCO 2000 Da, Millipore) and dialyzed for three days. Subsequently, the mixture was freeze-dried to obtain OCS and characterized using ^{1}H NMR spectroscopy (at 400 MHz, in D_2O, ppm).

The synthesis of HA-ADH was performed as follows: 1 g of hyaluronic acid was dissolved in 100 mL of distilled water and EDC/NHS (4 mmol: 4 mmol) was added at room temperature for 2 h to activate the carboxyl groups. Subsequently, 4 g of ADH was added, and the mixture was stirred for 24 h. The resulting solution was then transferred to a dialysis bag (MWCO 2000 Da, Millipore) and dialyzed for three days. The reaction solution was freeze-dried, and the product, HA-ADH, was characterized by 1H NMR spectroscopy (at 400 MHz, in D_2O, ppm).

To prepare the HACS hydrogel, 20 mg of OCS and HA-ADH were dissolved in 1 mL of PBS, respectively. A 100 μL solution of 2% OCS was mixed with a 400 μL solution of 2% HA-ADH to form the biomimetic hydrogels.

For HACS characterization, the morphology of hydrogels was observed by scanning electron microscopy (SEM) after freeze-drying. The compressive modulus was tested using the Miniature Multi-Scale In-Situ Mechanical Test System IBTC-300. The tensile property was tested using the Miniature Multi-Scale In-Situ Mechanical Test System IBTC-300. The samples were subjected to 50 cycles of compression to test their fatigue resistance properties.

The in vitro degradation was performed as follows: The initial net weight of the hydrogel samples (M0) was determined through vacuum freeze-drying. Then, the hydrogels were immersed in PBS (pH 5.5, pH 6.5 or pH 7.4) and incubated at 37 °C with gentle shaking. At specified time intervals, the hydrogels were extracted and freeze-dried, and their weight was recorded as M1. The degradation rate was calculated using the formula (M0-M1)/M0 × 100%.

Preparation and characterization of HACS@CPP-miR-Exo

For preparation of HACS@CPP-miR-Exo, 20 mg of OCS were dissolved in 1 mL of CPP-miR-Exo suspensions. Then, 20 mg of HA-ADH were dissolved in 1 mL of PBS, following mixed with OCS and CPP-miR-Exo solutions. The final concentration of exosomes of HACS@CPP-miR-Exo hydrogel was 200 μg/mL. The visualization of CPP-miR-Exo in HACS@CPP-miR-Exo hydrogel was performed by a Zeiss LSM880 confocal microscope. The morphology of HACS@CPP-miR-Exo was observed by SEM after freeze-drying.

Exosome release from the HACS@CPP-miR-Exo was measured via in vitro fluorescence imaging with an Imaging System (Newton, Viber Bio Imaging, France). Briefly, 1 mL of HACS@CPP-miR-Exo was added to the upper chamber of a 6-well Transwell plate with 2 mL of PBS in the lower chamber, following incubated at 37 °C with gentle shaking. Then, 100 μL of PBS in the lower chamber was collected for imaging at certain time points. The dissolution medium in the lower chamber was supplemented with fresh PBS.

In vivo targeting capability of HACS@CPP-miR-Exo for NPCs: HACS@CPP-miR-Exo or free CPP-miR-Exo was injected into the operated discs of IDD rats at a dose of 20 μL. The concentration of exosomes in both of the two groups were 200 ug/mL. Rats were performed in vivo fluorescence imaging at specified time points post-administration using an In Vivo Imaging System (Newton, Viber Bio Imaging, France).

Therapeutic evaluation of HACS@CPP-miR-Exo on IDD rats

IDD was induced in rats through vertically puncturing rat IVD with a microscalpel and the partial excise of NP using microscopic forceps. To examine the therapeutic efficacy of HACS@CPP-miR-Exo in IDD rats, equal volume of HACS, free CPP-miR-Exo, and HACS@CPP-miR-Exo were injected into the operated discs of different groups. Samples were injected into the NP defect. After removing the syringe, the wound was closed by suturing. At different time points (1 month and 2 months) after treatments, rats were euthanized. The IVDs were harvested for subsequent evaluation.

Safety studies

For in vitro studies, the cytotoxicity of the agents was assessed using the CCK-8 assay and calcein-AM/propidium iodide (PI) staining. In this study, NPCs were co-cultured with OCS, HA-ADH, and HACS in different concentrations for a duration of 3 days. For in vivo studies, HACS, free CPP-miR-Exo, and HACS@CPP-miR-Exo were injected into the operated discs of different experimental groups. At designated time points (2 months post-treatment), the rats were euthanized, and the IVDs were harvested for subsequent evaluation.

Radiological evaluation

MRI was performed on the rats 2 weeks after administration. Pfirrmann grading according to T2-weighted images was used to assess the degree of IDD[65].

Statistical analysis

Statistical analysis was performed using Origin software (OriginLab, U.S.A.). All quantitative data are expressed as the mean ± standard deviation (SD). The one-way analysis of variance (ANOVA) and two-tailed Student's t test followed by Tukey's honestly significant difference tests were performed for comparisons between the two groups. Two-way ANOVA followed by Tukey's honestly significant difference test was used to compare the behavioral data at different time points in more than two groups. A statistically significant difference was considered if the P value was less than 0.05.

Reporting summary

Further information on research design is available in the Nature Portfolio Reporting Summary linked to this article.

Data availability

All relevant data supporting the findings of this study are available within the article and its Supplementary Information files. Source Data are provided with this paper. The miRNA sequencing and RNA sequencing data are publicly available on the GEO database under accession code GSE290270 and GSE290271 [https://www.ncbi.nlm.nih.gov/geo/query/acc.cgi?acc=GSE290270 and https://www.ncbi.nlm.nih.gov/geo/query/acc.cgi?acc=GSE290271]. Source data are provided with this paper.

References

1. Fine, N. et al. Intervertebral disc degeneration and osteoarthritis: A common molecular disease spectrum. *Nat. Rev. Rheumatol.* **19**, 136–152 (2023).
2. Pan, M. et al. Percutaneous endoscopic lumbar discectomy: Indications and complications. *Pain. Phys.* **23**, 49–56 (2020).
3. Li, Y. et al. Adjuvant surgical decision-making system for lumbar intervertebral disc herniation after percutaneous endoscopic lumber discectomy: a retrospective nonlinear multiple logistic regression prediction model based on a large sample. *Spine J.* **21**, 2035–2048 (2021).
4. Aihara, T. et al. Five-year reoperation rates and causes for reoperations following lumbar microendoscopic discectomy and decompression. *Spine (Philos. Pa 1976)* **45**, 71–77 (2020).
5. Ru, Q. et al. Fighting age-related orthopedic diseases: focusing on ferroptosis. *Bone Res.* **11**, 12 (2023).
6. Zhang, Y. et al. Single-cell RNA-seq analysis identifies unique chondrocyte subsets and reveals involvement of ferroptosis in human intervertebral disc degeneration. *Osteoarthr. Cartil.* **29**, 1324–1334 (2021).
7. Zhu, J. et al. The deubiquitinase USP11 ameliorates intervertebral disc degeneration by regulating oxidative stress-induced ferroptosis via deubiquitinating and stabilizing Sirt3. *Redox Biol.* **62**, 102707 (2023).
8. Francisco, V. et al. A new immunometabolic perspective of intervertebral disc degeneration. *Nat. Rev. Rheumatol.* **18**, 47–60 (2022).
9. Gao, B. et al. Discovery and application of postnatal nucleus pulposus progenitors essential for intervertebral disc homeostasis and degeneration. *Adv. Sci. (Weinh.)* **9**, e2104888 (2022).
10. Zhou T. et al. Spatiotemporal characterization of human early intervertebral disc formation at single-cell resolution. *Adv Sci (Weinh)*, **10**, e2206296 (2023).
11. Gan, Y. et al. Spatially defined single-cell transcriptional profiling characterizes diverse chondrocyte subtypes and nucleus pulposus progenitors in human intervertebral discs. *Bone Res.* **9**, 37 (2021).
12. Xia, K. S. et al. An esterase-responsive ibuprofen nano-micelle premodified embryo derived nucleus pulposus progenitor cells promote the regeneration of intervertebral disc degeneration. *Bioact. Mater.* **21**, 69–85 (2023).
13. Lyu, F. J. et al. IVD progenitor cells: A new horizon for understanding disc homeostasis and repair. *Nat. Rev. Rheumatol.* **15**, 102–112 (2019).
14. Fontana, G., See, E. & Pandit, A. Current trends in biologics delivery to restore intervertebral disc anabolism. *Adv. Drug Deliv. Rev.* **84**, 146–158 (2015).
15. Tan, Z. et al. Progenitor-like cells contributing to cellular heterogeneity in the nucleus pulposus are lost in intervertebral disc degeneration. *Cell Rep.* **43**, 114342 (2024).
16. Thompson, J. P. et al. Preliminary evaluation of a scheme for grading the gross morphology of the human intervertebral disc. *Spine (Philos. Pa 1976)* **15**, 411–415 (1990).
17. Shu, H. S. et al. Tracing the skeletal progenitor transition during postnatal bone formation. *Cell Stem Cell* **28**, 2122–2136.e2123 (2021).
18. Farup, J. et al. Human skeletal muscle CD90(+) fibro-adipogenic progenitors are associated with muscle degeneration in type 2 diabetic patients. *Cell Metab.* **33**, 2201–2214.e2211 (2021).
19. Wu, J., Li, Z., Wu, Y. & Cui, N. The crosstalk between exosomes and ferroptosis: a review. *Cell Death Discov.* **10**, 170 (2024).
20. Chen, L. et al. Mesenchymal stem cell-derived extracellular vesicles protect against abdominal aortic aneurysm formation by inhibiting NET-induced ferroptosis. *Exp. Mol. Med.* **55**, 939–951 (2023).
21. Lin, F. et al. Mesenchymal stem cells protect against ferroptosis via exosome-mediated stabilization of SLC7A11 in acute liver injury. *Cell Death Dis.* **13**, 271 (2022).
22. Li, C. et al. Roles and mechanisms of exosomal non-coding RNAs in human health and diseases. *Signal Transduct. Target Ther.* **6**, 383 (2021).
23. Wei, Z. et al. Human umbilical cord mesenchymal stem cells derived exosome shuttling mir-129-5p attenuates inflammatory bowel disease by inhibiting ferroptosis. *J. Nanobiotechnol.* **21**, 188 (2023).
24. Shen, K. et al. miR-125b-5p in adipose derived stem cells exosome alleviates pulmonary microvascular endothelial cells ferroptosis via Keap1/Nrf2/GPX4 in sepsis lung injury. *Redox Biol.* **62**, 102655 (2023).
25. Qi, R. et al. Cancer-associated fibroblasts suppress ferroptosis and induce gemcitabine resistance in pancreatic cancer cells by secreting exosome-derived ACSL4-targeting miRNAs. *Drug Resist Updat* **68**, 100960 (2023).
26. Sone, H. et al. MicroRNA-mediated attenuation of branched-chain amino acid catabolism promotes ferroptosis in chronic kidney disease. *Nat. Commun.* **14**, 7814 (2023).
27. Mikami, Y. et al. MicroRNA-221 and -222 modulate intestinal inflammatory Th17 cell response as negative feedback regulators downstream of interleukin-23. *Immunity* **54**, 514–525.e516 (2021).
28. Olivieri, F. et al. miR-21 and miR-146a: The microRNAs of inflammaging and age-related diseases. *Ageing Res. Rev.* **70**, 101374 (2021).
29. Wei, C. et al. Exosomal miR-181d-5p derived from rapamycin-conditioned MDSC alleviated allograft rejection by targeting KLF6. *Adv. Sci. (Weinh.)* **10**, e2304922 (2023).
30. Deng Z. et al. Mesenchymal stem cells prevent SLC39A14-dependent hepatocyte ferroptosis through exosomal miR-16-5p in Liver Graft. *Adv. Sci. (Weinh)*, **12**, e2411380 (2024).
31. Shi, X. et al. A simple polydopamine-based platform for engineering extracellular vesicles with brain-targeting peptide and imaging probes to improve stroke outcome. *J. Extracell. Vesicles* **14**, e70031 (2025).
32. Singh, A. K. et al. Global microRNA expression profiling in the liver biopsies of hepatitis B virus-infected patients suggests specific microRNA signatures for viral persistence and hepatocellular injury. *Hepatology* **67**, 1695–1709 (2018).
33. Zhang, Z. et al. Transfer of MicroRNA via macrophage-derived extracellular vesicles promotes proneural-to-mesenchymal transition in glioma stem cells. *Cancer Immunol. Res.* **8**, 966–981 (2020).
34. Hong, J. et al. The PRMT6/STAT1/ACSL1 axis promotes ferroptosis in diabetic nephropathy. *Cell Death Differ.* **31**, 1561–1575 (2024).
35. Kong, P. et al. Ferroptosis triggered by STAT1- IRF1-ACSL4 pathway was involved in radiation-induced intestinal injury. *Redox Biol.* **66**, 102857 (2023).
36. Tao, Q. et al. Mefloquine enhances the efficacy of anti-PD-1 immunotherapy via IFN-γ-STAT1-IRF1-LPCAT3-induced ferroptosis in tumors. *J. Immunother. Cancer* **12**, e008554 (2024).
37. Wan, C. et al. Irradiated tumor cell-derived microparticles mediate tumor eradication via cell killing and immune reprogramming. *Sci. Adv.* **6**, eaay9789 (2020).

38. Szklarczyk, D. et al. The STRING database in 2023: Protein-protein association networks and functional enrichment analyses for any sequenced genome of interest. *Nucleic Acids Res.* **51**, D638–d646 (2023).
39. Philips, R. L. et al. The JAK-STAT pathway at 30: Much learned, much more to do. *Cell* **185**, 3857–3876 (2022).
40. Zimmerman, M. A. et al. Unphosphorylated STAT1 promotes sarcoma development through repressing expression of Fas and bad and conferring apoptotic resistance. *Cancer Res.* **72**, 4724–4732 (2012).
41. Xiao, T., Li, X. & Felsenfeld, G. The Myc-associated zinc finger protein epigenetically controls expression of interferon-γ-stimulated genes by recruiting STAT1 to chromatin. *Proc. Natl. Acad. Sci. USA* **121**, e2320938121 (2024).
42. Langlais, D., Barreiro, L. B. & Gros, P. The macrophage IRF8/IRF1 regulome is required for protection against infections and is associated with chronic inflammation. *J. Exp. Med.* **213**, 585–603 (2016).
43. Kulkarni, J. A. et al. The current landscape of nucleic acid therapeutics. *Nat. Nanotechnol.* **16**, 630–643 (2021).
44. Torchilin, V. P. Tat peptide-mediated intracellular delivery of pharmaceutical nanocarriers. *Adv. Drug Deliv. Rev.* **60**, 548–558 (2008).
45. Tietz, O., Cortezon-Tamarit, F., Chalk, R., Able, S. & Vallis, K. A. Tricyclic cell-penetrating peptides for efficient delivery of functional antibodies into cancer cells. *Nat. Chem.* **14**, 284–293 (2022).
46. Joshi, B. S., de Beer, M. A., Giepmans, B. N. G. & Zuhorn, I. S. Endocytosis of extracellular vesicles and release of their cargo from endosomes. *ACS Nano* **14**, 4444–4455 (2020).
47. Mulcahy L. A., Pink R. C. & Carter D. R. Routes and mechanisms of extracellular vesicle uptake. *J. Extracell Vesicles* **3**, 24641 (2014).
48. Mathieu, M., Martin-Jaular, L., Lavieu, G. & Théry, C. Specificities of secretion and uptake of exosomes and other extracellular vesicles for cell-to-cell communication. *Nat. Cell Biol.* **21**, 9–17 (2019).
49. Kreiner, D. S. et al. An evidence-based clinical guideline for the diagnosis and treatment of lumbar disc herniation with radiculopathy. *Spine J.* **14**, 180–191 (2014).
50. Qin, L., Jiang, X., Zhao, S., Guo, W. & You, D. A Comparison of Minimally Invasive Surgical Techniques and Standard Open Discectomy for Lumbar Disc Herniation: A Network Meta-analysis. *Pain. Physician* **27**, E305–e316 (2024).
51. Jiang, X., Stockwell, B. R. & Conrad, M. Ferroptosis: mechanisms, biology and role in disease. *Nat. Rev. Mol. Cell Biol.* **22**, 266–282 (2021).
52. Tan, F. et al. Clinical applications of stem cell-derived exosomes. *Signal Transduct. Target Ther.* **9**, 17 (2024).
53. Zhou, X. et al. The function and clinical application of extracellular vesicles in innate immune regulation. *Cell Mol. Immunol.* **17**, 323–334 (2020).
54. Kalluri, R. & LeBleu, V. S. The biology, function, and biomedical applications of exosomes. *Science* **367**, eaau6977 (2020).
55. Kimiz-Gebologlu, I. & Oncel, S. S. Exosomes: Large-scale production, isolation, drug loading efficiency, and biodistribution and uptake. *J. Control Release* **347**, 533–543 (2022).
56. Fan, M. H. et al. Hydrogel-exosome system in tissue engineering: A promising therapeutic strategy. *Bioact. Mater.* **38**, 1–30 (2024).
57. Yu, H. et al. Stimulus-responsive hydrogels as drug delivery systems for inflammation targeted therapy. *Adv. Sci. (Weinh.)* **11**, e2306152 (2024).
58. Han, X. et al. Exosome-coated oxygen nanobubble-laden hydrogel augments intracellular delivery of exosomes for enhanced wound healing. *Nat. Commun.* **15**, 3435 (2024).
59. Liu, Y. et al. High-performance hydrogel-encapsulated engineered exosomes for supporting endoplasmic reticulum homeostasis and boosting diabetic bone regeneration. *Adv. Sci. (Weinh.)* **11**, e2309491 (2024).
60. Cui, Y. et al. Melatonin engineering M2 macrophage-derived exosomes mediate endoplasmic reticulum stress and immune reprogramming for periodontitis therapy. *Adv. Sci. (Weinh.)* **10**, e2302029 (2023).
61. Wei, J. R. et al. Neural cell isolation from adult macaques for high-throughput analyses and neurosphere cultures. *Nat. Protoc.* **18**, 1930–1957 (2023).
62. Ackermann, M. et al. Continuous human iPSC-macrophage mass production by suspension culture in stirred tank bioreactors. *Nat. Protoc.* **17**, 513–539 (2022).
63. Tan, J. J. et al. Human iPS-derived pre-epicardial cells direct cardiomyocyte aggregation expansion and organization in vitro. *Nat. Commun.* **12**, 4997 (2021).
64. Liu, L. et al. Gli1 depletion induces oxidative stress and apoptosis of nucleus pulposus cells via Fos in intervertebral disc degeneration. *J. Orthop. Transl.* **40**, 116–131 (2023).
65. Pfirrmann, C. W., Metzdorf, A., Zanetti, M., Hodler, J. & Boos, N. Magnetic resonance classification of lumbar intervertebral disc degeneration. *Spine (Philos. Pa 1976)* **26**, 1873–1878 (2001).

Acknowledgements

This study was supported by the National Natural Science Foundation of China (82472445 to M.H. Liu, 32471457 to Z.L., 32122048 to Z.L., 52333011 to Z.L., 2022YFB3804400 to Z.L., and 52471261 to Y.H.), the Natural Science Foundation of Chongqing (CSTB2022NSCQ-MSX1366 to M.H.Liu, CSTB2022NSCQ-MSX0488 to Y.H., cstc2021jcyj-cxttX0002 to Z.L. and 2023NSCQ-MSX3661 to Z.L.), the Fundamental Research Funds for the Central Universities (2024CDJXY016 to M.H.Li, 2024CDJYXTD-008 to Z.L., 2023CDJYGRH-ZD01 to Z.L. and 2023CDJYGRH-YB01 to Y.H.), the Chongqing Municipal Education Commission (0304005401108 to Z.L.), and the Chongqing Talents Program (cstc2024ycjh-bgzxm0031 to M.H.Liu).

Author contributions

W.K. W. and Z. C. contributed equally to this work. M.H.Liu, Z. L. and Y.H. conceived the project. M.H.Liu, W.K. W., and Z. C. designed the experiments. W.K. W., Z.C., M.Y., K.L., H.L. D., Y.Z., and X.L.H. performed the experiments. W.K. W., Z. C., M.H. Li, and C.Q. L. analyzed and interpreted the data. M.H. Liu, W.K.W., Z.L. and Y.H. wrote the manuscript. M.H.Liu, Z.L. and Y.H. supervised this study. All authors discussed the results and reviewed the manuscript.

Competing interests

The authors declare no competing interests.

Additional information

Supplementary information The online version contains supplementary material available at https://doi.org/10.1038/s41467-025-58447-5.

Correspondence and requests for materials should be addressed to Yan Hu, Zhong Luo or Minghan Liu.

Peer review information *Nature Communications* thanks the anonymous reviewers for their contribution to the peer review of this work. A peer review file is available.